Numerical Simulation of the Start and Unstart Behaviour of a Ram- or Scramjet

Master's Thesis

by

Adrian Thomas Esteban Krieger

Referees DLR: Dr.-Ing. Andreas Flock, Prof. Dr.-Ing. Ali Gülhan

Referee RWTH: Prof. Dr.-Ing. Herbert Olivier

The present work was submitted to the Shock Wave Laboratory

RWTH Aachen University

27th September 2019

Preface

First of all, I want to express my gratitude to Prof. Gülhan, the head of the Supersonic and Hypersonic Technology Department of the German Aerospace Center (DLR) in Cologne, for offering me the opportunity to work on this interesting topic in the inspiring environment of DLR and for providing me with excellent conditions.
Moreover, I would like to thank Prof. Olivier, head of the Shock Wave Laboratory at RWTH Aachen University, for supervising my work, for supporting me with his experience and for his interest in my thesis.
My very special thanks go to my supervisor Dr. Andreas Flock for his dedicated and continuous support during our weekly meetings and every other time I asked for his advice, for his stimulating ideas and last but not least his confidence in me and my work.
Furthermore, I would like to thank Dr. Dirk Herrmann and Martin Achner for supplying me with experimental data and for performing additional tests to support this work.
Additionally, I would like to thank the department for the congenial and fostering working atmosphere and numerous valuable contributions. Exemplary, I would like to thank Dr. Burkard Esser for his support on IT related issues and our fruitful conversations about numeric and fluid dynamics.
Finally, I would like to thank my friends and family – especially my parents – for their encouragement and for the revisions of my thesis.

Contents

List of Figures

Nomenclature

A	area	m^2
A^*	critical area	m^2
c	flow velocity	$\mathrm{m/s}$
C_F	constant in Flock's criterion	
C_F	relative wall temperature constant	
C_μ	constant in Sutherland's law	
$C_{\omega 1}$, $C_{\omega 2}$, $C_{\omega 3}$,	Constants in k-ω model	
CFL	Courant-Friedrich-Levy number	
CR	contraction ratio	
F	Thrust	$\mathrm{kg \cdot m/s}^2$
g	gravity constant	$\mathrm{m/s}^2$
h	specific enthalpy	$\mathrm{m}^2/\mathrm{s}^2$
h	altitude	m
I_{sp}	specific impulse	s
k	mean specific turbulent kinetic energy	$\mathrm{m}^2/\mathrm{s}^3$
k	thermal conductivity	$\mathrm{W/(m \cdot K)}$
L	characteristic length	m
M	Mach number	
MCR	mass capture ratio	
$\dot{m}$	mass flow rate	$\mathrm{kg/s}$
n	natural number	
p	pressure	$\mathrm{N/m}^2$
Pr	Prandtl number	
q	dynamic pressure	$\mathrm{N/m}^2$
R	universal gas constant	$\mathrm{J/(mol \cdot K)}$
Re	Reynolds number	
Re_u	unit Reynolds number	m^{-1}
Res	Residual	
r	radius	m
T	temperature	K
T_r	reference temperature	K
u	velocity	$\mathrm{m/s}$
x, y, z	coordinates	m
x_c	position of cone tip	m
y^+	non-dimensional wall distance	
α	pitch angle	$^\circ$
β	shock angle	$^\circ$
γ	heat capacity ratio	
δ	Kronecker Delta	
ε	turbulent rate of dissipation	$\mathrm{m}^2/\mathrm{s}^3$
Θ	temperature ratio	
θ	deflection angle	$^\circ$
μ	dynamic viscosity	$\mathrm{kg/(m \cdot s)}$
μ_r	reference dynamic viscosity	$\mathrm{kg/(m \cdot s)}$

ν	kinematic viscosity	m^2/s
Π	pressure ratio	
ρ	density	kg/m^3
τ_{tu}	Reynolds stress tensor	$\mathrm{kg}/(\mathrm{s}^2 \cdot \mathrm{m})$
τ_{w}	wall shear stress	$\mathrm{kg}/(\mathrm{s}^2 \cdot \mathrm{m})$
ω	dissipation per unit turbulent kinetic energy	$\mathrm{m}^2/\mathrm{s}^3$

Subscripts

0	at capture area
1	upstream of shock
2	downstream of shock
2D	two-dimensional case
c	cone
cc	combustion chamber
cl	cowl tip
DP	design point
e	edge of boundary layer
emp	empirical
Isent	Isentropic
i, j	index variables
Kantr	Kantrowitz
n	normal to shock
p	propellant
r	ramp-tip
s	static or local condition
sp	specific
t	total or stagnation condition
th	throat
tr	transition
tu	turbulent
vWie	van Wie
w	wall
we	wedge
∞	free stream condition

Abbreviations

AEX1D	Automatic extract 1D
AUSMDV	Advection Upstream Splitting Method in DV-Version
AoA	Angle of Attack
BMAP	Boundary-Mapping
CFD	Computational Fluid Dynamics
CFL	Courant-Friedrichs-Lewy
DLR	German Aerospace Center
DNS	Direct Numerical Simulation
HySIF	Hysteresis of Supersonic Intake Flows
LES	Large Eddy Simulation
RANS	Reynolds-Averaged Navier-Stokes
SAO	Spalart-Allmaras model in the O-version

SING2D	Supersonic Intake Design 2D
SST	Shear Stress Transport
TMK	Trisonic Test Section Cologne
WT	Wind Tunnel

Abstract

Ram- and Scramjets have the potential to enable super- and hypersonic ground to ground travel and to reduce costs for access to orbit. Both engines use atmospheric air as oxidizer, which is compressed by the ram effect. For this purpose, the intake must provide a sufficient pressure level for combustion over a wide range of Mach numbers while producing minimal drag. Critical processes during the operation of Ram- and Scramjets are the formation (starting) and the breakdown (unstarting) of the desired shock configuration in the intake. Whereas started intake flow is crucial for efficient operation, unstarting causes aerothermal and mechanical loads. Thereby, accidental unstart can lead to loss of the vehicle, and thus has to be prevented.

This study focuses on the numerical prediction of starting and unstarting in dependence of the free stream Mach number and the angle of attack. Therefore, a quasi-steady numerical approach has been developed, which reduces computational costs compared to unsteady approaches. In order to predict starting and unstarting, a set of subsequent steady-state simulations is performed. Each simulation is based on the previous results with a slightly varied free stream Mach number or angle of attack. This approach has been applied to intakes with mixed internal and external compression, namely generic two-dimensional ramp intakes and an axisymmetric intake with movable centerbody. The approach was validated with experiments for the axisymmetric intake, which demonstrated that numerical simulations predicted critical Mach numbers for starting and unstarting within 10% accuracy. Furthermore, a parameter study was carried out, to analyze the effects of Reynolds number and relative wall temperature. It was found that a threshold exists for independence of Reynolds number and relative wall temperature on the starting Mach number. Finally, it was found that a flight trajectory with constant dynamic pressure reduced critical Mach numbers for starting and unstarting by up to 5% compared to simulated wind tunnel conditions.

1 Introduction

1.1 Application of Ram- and Scramjets

Conventional jet engines work efficiently in subsonic and lower supersonic flow regimes. For supersonic application of jet engines, the flow has to be decelerated to subsonic speeds upstream of the compressor in order to reduce shock losses in the rotating turbo-machinery. The deceleration is accomplished in the intake via shocks, which increase pressure and temperature of the flow. For higher Mach numbers, the compressor operates increasingly inefficient and temperatures become too high for the rotating parts. Furthermore, the high temperatures lead to dissociation of flow molecules, thus reducing the efficiency of the cycle [31].

Ram- and Scramjets omit the turbo-machinery, thus the necessary pressure for efficient combustion is solely generated via compression shocks produced by supersonic inflow [32]. Whereas Ramjets decelerate the flow to subsonic speeds in the combustion chamber, the combustion in Scramjets takes place at supersonic speeds, from which the name "Supersonic Combustion Ramjet engine" is derived. Shock losses are reduced if the flow is not decelerated to subsonic speeds, thus increasing the efficiency of Scramjets over Ramjets at high Mach numbers. The scramjet intake must therefore provide the necessary pressure level for efficient combustion without decelerating the flow to subsonic speeds. If that succeeds, a Scramjet engine can work efficiently at higher Mach numbers and thus extend the accessible range to high hypersonic speeds as depicted in figure 1.1 a) [31].

The other feasible option to propel a vehicle to hypersonic speeds are rockets. In contrast to them, Ram- and Scramjets use atmospheric oxygen as oxidizer. Since liquid oxygen accounts for a significant portion of a rocket's take-off mass (i.e. roughly two thirds for the Saturn V [15]), spacecraft propelled by Ram- and Scramjets have significantly better propellant mass fraction [15]. Furthermore, airbreathing engines are more efficient than rockets, which is described by the specific impulse I_{sp}, which relates the produced thrust F to the propellant mass flow $\dot{m}_{\mathrm{p}}$ and the gravitational constant g:

$$I_{sp} = \frac{F}{g\,\dot{m}_{\mathrm{p}}} \tag{1.1}$$

Since airbreathing engines only carry fuel and no oxidizer, their propellant mass flow is constituted only by the fuel mass flow and thus their specific impulse is much larger than for equivalent rockets (see fig. 1.1 a)) [31]. Therefore, Ram- and Scramjets promise to enable efficient super- and hypersonic cruising within the atmosphere. Thereby, they would allow for new possibilities of access to orbit and for hypersonic ground to ground travel.

However, the operation of Ram- and Scramjets is limited to the lower atmosphere, where oxygen is abundant. Additionally, the vehicle must initially be propelled to a take-over-velocity, in order for the ram effect to be sufficiently strong. This leads to trajectories with multiple propulsion technologies. An exemplary trajectory for access to orbit is shown in figure 1.1 b).

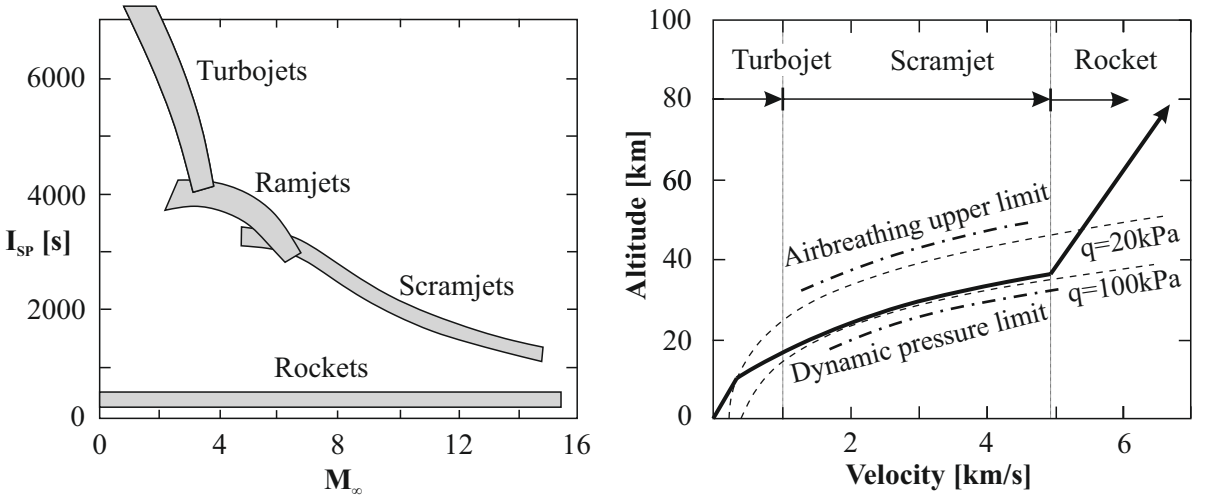

a) Propulsion systems b) Airbreathing trajectory

Figure 1.1: Propulsion systems (a) and potential trajectory of Scramjet-powered access to orbit (b) both according to [31]

Ramjets have already been successfully applied in the SR-71 aircraft alias Blackbird (retired) and several missiles [15]. The Scramjet technology, however, has not yet made it past early prototype stage. Several of these flight experiments were subject of accidental unstart [9], like within the X-51A project, that later set the record for the longest self-sustained hypersonic flight. Clearly, the problem of unstarting is not fully understood to this point and further research is needed.

1.2 Aerodynamic Fundamentals

1.2.1 Quasi-One-Dimensional Flow

For simple problems like the transonic internal flow through a convergent-divergent nozzle, analytical solutions have been developed. Although internal flows with varying flow area A are in general three-dimensional, the flow can be treated as quasi-one-dimensional if the change of area is gradual [4].
Assuming a calorically perfect gas, quasi-one-dimensional, steady, adiabatic and isentropic flow, the Mach Number M can be expressed only as function of the ratio between the local cross section A and the critical cross section A^*, where $M = 1$:

$$\frac{A}{A^*} = \frac{1}{M}\left[\frac{2}{\gamma+1}\left(1+\frac{\gamma-1}{2}M^2\right)\right]^{\frac{\gamma+1}{2(\gamma-1)}} \tag{1.2}$$

This equation has to be solved iteratively. The relation between local and total flow properties are themselves functions of the Mach Number [4, p.59]:

$$\frac{T}{T_\mathrm{t}} = \frac{p}{p_\mathrm{t}}^{\frac{\gamma-1}{\gamma}} = \frac{\rho}{\rho_\mathrm{t}}^{\gamma-1} = \left(1+\frac{\gamma-1}{2}M^2\right)^{-1} \tag{1.3}$$

Consequently, the ratios between local and total flow properties can also be related to the area ratio.
While being a useful tool for fast analysis of internal supersonic flows, the theory is limited to isentropic flow. Therefore, viscous effects are not covered and the theory cannot be (directly) applied across shocks [4, pp. 147ff.].

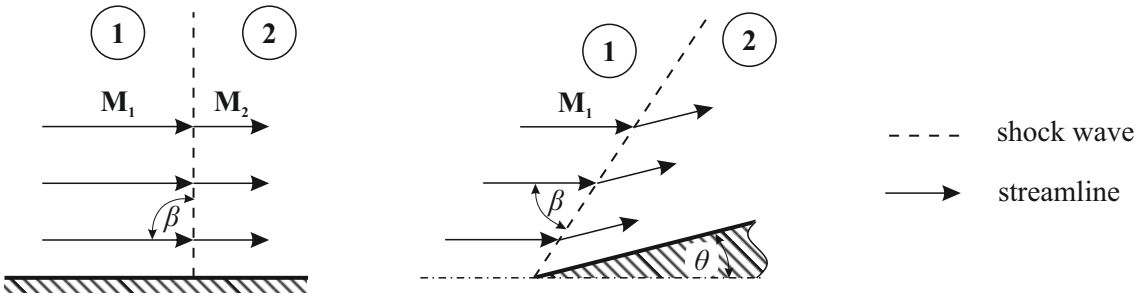

a) normal shock b) oblique shock (2D)

Figure 1.2: Two-dimensional flow across normal shock and oblique shock

1.2.2 Shock Relations

Shocks are always irreversible and thus cannot be analyzed with the presented quasi-one-dimensional approach. For analytical approaches, shocks are treated as discontinuities that divide the flow field into an up- (1) and a downstream (2) region. Furthermore, steady flow of a calorically perfect gas is assumed. For a given deflection angle $\theta < \theta_{\max}$ and upstream Mach Number $M_1 > 1$, the shock angle β can be calculated via the θ-β-M relation:

$$\tan(\theta) = 2\cot(\beta)\left[\frac{M_1^2\sin^2(\beta) - 1}{M_1^2(\gamma + \cos(2\beta)) + 2}\right] \tag{1.4}$$

There exist two solutions for β depending on the back pressure, which are denoted as strong and weak shock. Strong shocks cause stronger compression and subsonic downstream flow, whereas weak shocks usually produce supersonic downstream flow [4, p.107ff.]. Normal shocks can be treated as special case of oblique shocks with $\beta = \pi/2 = 90°$. Consequently, the other flow parameters can be calculated across the shock:

$$M_{\mathrm{n1}} = M_1\sin(\beta) \tag{1.5}$$

$$\frac{p_2}{p_1} = 1 + \frac{2\gamma}{\gamma+1}(M_{\mathrm{n1}}^2 - 1) \tag{1.6}$$

$$\frac{\rho_2}{\rho_1} = \frac{(\gamma+1)M_{\mathrm{n1}}^2}{(\gamma-1)M_{\mathrm{n1}}^2 + 2} \tag{1.7}$$

$$\frac{T_2}{T_1} = \frac{p_2}{p_1}\frac{\rho_2}{\rho_1} \tag{1.8}$$

$$M_2 = \frac{M_{\mathrm{n},2}}{\sin(\beta - \theta)} \tag{1.9}$$

Across a steady shock, total temperature is constant. However, total pressure is reduced.

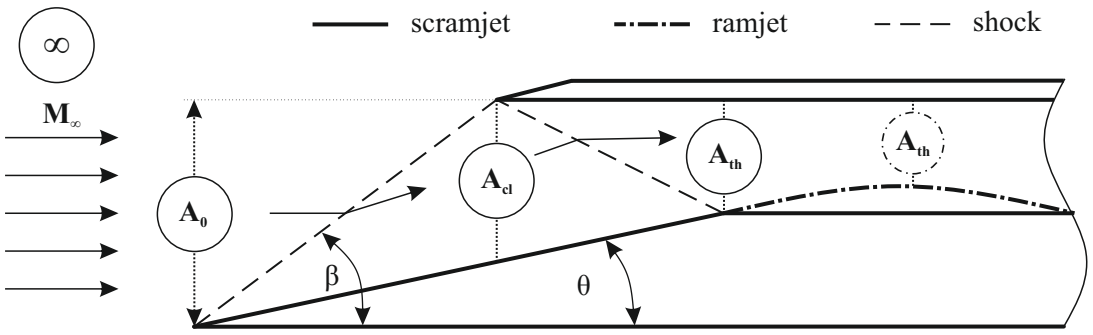

Figure 1.3: Simplified flow field of Ram- (dotted) and Scramjet intake with combined internal and external compression in started mode.

1.2.3 Ram- and Scramjet Intake Flows

The purpose of Ram- and Scramjet intakes is to provide the necessary pressure for efficient combustion while producing a minimum of aerodynamic losses. In contrast to conventional jet engines, rotating parts are omitted and pressure is increased solely by aerodynamic means namely shocks, deceleration via contraction and viscous losses. The compression can be done externally, internally or combined. Within this work, intakes with mixed internal-external compression and freestream-parallel outflow are investigated.

A general flow field of these intakes is presented in figure 1.3. Upstream of the intake, the flow is at ambient conditions (∞). The maximum capture area A_0 contains all streamlines that can potentially enter the internal flow at supersonic conditions. The streamlines get deflected by one or more ramp shocks and a concluding shock emanating from the cowl tip. The cowl area A_{cl} marks the beginning of the internal flow and is used to compare intakes with and without external compression. The convergent intake region is concluded by the throat area A_{th}.

Upstream of the throat area, the principal design of Ram- and Scramjets is similar, but differs downstream of it. On the one hand, Ramjets contain a divergent region downstream of the throat area, that allows a strong shock to be stable [16], which creates subsonic flow for the combustion. In Scramjets, on the other hand, the throat area is directly followed by the isolator, that is supposed to decouple intake from combustion [31].

The flow around axisymmetric intakes differs from two-dimensional flows due to a three-dimensional relieving effect [4]: Whereas the flow downstream of two-dimensional shocks is uniform, the flow downstream of conical shocks is subject to a continuous isentropic compression. However, the compression directly across a shock with a given shock angle β is equal for conical and two-dimensional shocks as depicted in figure 1.4. Therefore, immediately downstream of the shock, the deflection angle θ is equal for two-dimensional and conical shocks assuming equal β and equals the corresponding wedge angle δ_{we}. The local flow deflection behind the shock θ_{c} is smaller than the cone angle δ_{c} and, only in the limit of infinite cone length, the local flow angle approaches δ_{c}. Consequently, the flow field downstream of a conical shock is non-uniform opposed to the uniform flow field downstream of a two-dimensional shock. Besides producing non-uniformity, the three-dimensionality also increases the cone angle δ_{c} that leads to a given shock angle β compared to wedge flow [16, pp. 255ff.].

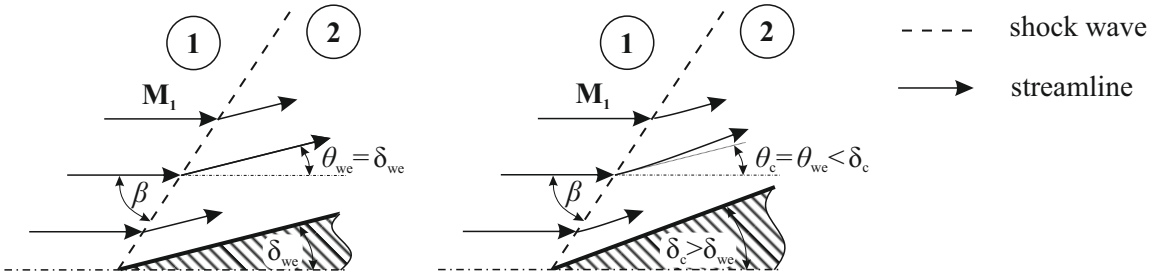

a) oblique wedge shock (2D) b) oblique conical shock

Figure 1.4: Flow across an oblique wedge shock (a) and across an oblique conical shock (b) for equal shock angle β

Similarity Parameters

In order to transfer findings to similar flows, similarity parameters are introduced: For viscous compressible flows, the governing similarity parameters are the Mach number M, the Reynolds number Re, the Prandtl number Pr and the ratio of the specific heats γ [5, p.662]:

$$M = \frac{u}{a} = \frac{u}{\sqrt{\gamma RT}} \propto \frac{\text{flow kinetic energy}}{\text{flow internal energy}} \tag{1.10}$$

$$Re = \frac{\rho u L}{\mu} \propto \frac{\text{inertia forces}}{\text{viscous forces}} \tag{1.11}$$

$$Pr = \frac{\mu c_p}{k} \propto \frac{\text{frictional dissipation}}{\text{thermal conduction}} \tag{1.12}$$

$$\gamma = \frac{c_p}{c_v} \tag{1.13}$$

Where a is the local speed of sound, R is the specific gas constant, L is the characteristic length of the analyzed phenomenon, μ is the dynamic viscosity of the fluid c_p and c_v are the specific heats at constant pressure and constant density respectively and k is the thermal conductivity.

Additionally, the dynamic pressure q shall be introduced:

$$q = \frac{\rho}{2} v^2 \tag{1.14}$$

The dynamic pressure is not a similarity parameter, but is a scaling factor for aerodynamic forces and used to deduce super- and hypersonic trajectories. [15, pp. 37f.]

Performance Parameters

Intakes can significantly differ in their design and often contain highly complex flow fields. In order to compare the performance of different intakes or flow conditions, non-dimensional performance parameters are introduced according to their formulation in [12]:

Static pressure ratio $\Pi_s = p/p_\infty$ is the central performance requirement for the intake design. It is directly correlated to combustion efficiency [32].

Total pressure ratio $\Pi_\mathrm{t} = p_\mathrm{t}/p_{\mathrm{t},\infty}$ acts as an indicator for aerodynamic losses. Within an intake the total pressure ratio can vary between $0 < \Pi_\mathrm{t} < 1$, higher values representing higher efficiency.

Static temperature ratio $\Theta_\mathrm{s} = T/T_\infty$ is also related to the intake's efficiency.

Total temperature ratio $\Theta_\mathrm{t} = T_\mathrm{t}/T_{\mathrm{t},\infty}$ serves as indicator for heat transfer into the flow, since the flow's total temperature only changes if heat is exchanged with its surrounding. Hence, Θ_t indicates, whether the flow is cooled ($\Theta_\mathrm{t} < 1$), heated ($\Theta_\mathrm{t} > 1$) or adiabatic ($\Theta_\mathrm{t} = 1$).

Mass capture ratio $MCR = \dot{m}_\mathrm{cl}/\dot{m}_0$ relates the mass flow to the maximum possible mass flow. Since thrust is a function of the mass flow, it is usually opted for $MCR \approx 1$ for operation at design conditions.

Total contraction ratio $CR = A_0/A_\mathrm{th}$ relates the capture area A_0 to the throat area A_th of an intake. It is a geometrical parameter and thus independent of the flow conditions.

Internal contraction ratio $CR_\mathrm{i} = A_\mathrm{cl}/A_\mathrm{th}$ is the ratio between the entry plane of the internal flow A_cl and the throat area A_th. For intakes with only internal compression, $CR_\mathrm{i} = CR$ holds. CR_i has proven to be one of the dominant parameters of intake starting and unstarting [32]. These performance parameters allow for a meaningful comparison of various geometries or flow fields if applied to characteristic cross sections (like A_cl, A_th etc.).

1.2.4 Starting and Unstarting

For supersonic intakes there exist two main flow-modes which are mostly denoted as started and unstarted mode. Since there are several sub-modes of unstarted flow [9], a general definition of started flow by van Wie is utilized: An intake is started, if the internal flow does not affect the capture characteristics of the intake. Every other flow condition is referred to as unstarted [40].

Started and unstarted mode can be simultaneously stable for specific flow conditions. In that case, the unstarted mode captures less air while higher aerodynamic losses are produced. Therefore, thrust, that is proportional to the mass flow, is reduced and drag is increased for unstarted flow conditions. Furthermore, the structure is exposed to high and potentially oscillatory aerothermal loads [37]. This is why the prediction of the starting and unstarting is an essential field of research for the development of Ram- and Scramjets.

Phenomenology

During the process of starting and unstarting, a shock or a shock-system is swallowed (starting) or expelled (unstarting) by the internal portion of the intake. These processes take place within extremely low time scales in the order of milliseconds [10, 14], making it difficult if not impossible to stop the process, if the transition has already begun. The reason for the rapidity of the change of modes is that the shock or shock system is unstable within the convergent part of the intake [16].

The started flow field is predominantly supersonic at the beginning of the internal section (A_cl) of the intake. Thus, the external flow is not affected by the internal flow. However, unstarted flow fields contain significant portions of subsonic flow at A_cl, so pressure waves can propagate upstream, coupling internal and external flow fields. This coupling potentially evokes oscillatory flow behavior, which is denoted as "buzz" [37].

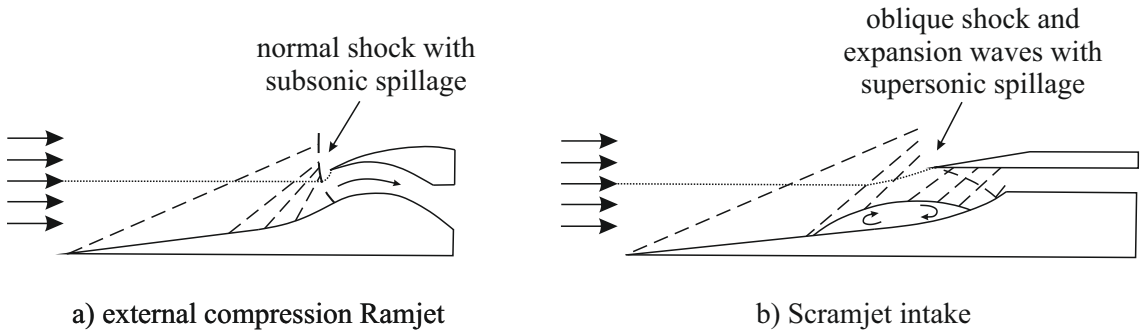

Figure 1.5: Different unstart modes (adapted from [40])

As depicted in figure 1.5 unstart can be divided into two main cases: Unstart with a normal shock (a) and unstart with an oblique shock that emanates from a separation bubble (b). Unstarts with normal shock typically appear within flows in Ramjets, where the boundary layer is typically small compared to the area of the intake. The normal shock induces subsonic flow at A_{cl} and within the spillage mass flow. For hypersonic flows in Scramjet intakes, the boundary layer can account for a significant portion of the flow. These boundary layers are prone to separation, thus leading to the unstart-mode with an oblique shock. The weak oblique shock upstream of the boundary layer separation deflects the flow outwards, resulting in a supersonic spillage flow and a partially supersonic flow at A_{cl} [40].

Acting Parameters

Starting and unstarting of supersonic intakes are dependent on geometrical features of the intake, external flow characteristics and the downstream engine process. The dominant geometrical parameter has been found to be the internal contraction ratio CR_{i}. As for the external flow, free stream Mach number M_∞ and angle of attack α are important, since they, in interaction with the geometry, control the Mach number at the cowl area M_{cl}. Furthermore, unstart can be caused by back pressure that is induced by the combustion [9, 40].

Additionally, boundary layer parameters affect starting and unstarting [10, 14, 40]. Therefore, the similarity parameters of super- and hypersonic boundary layers, especially Re and $T_{\mathrm{e}}/T_{\mathrm{w}}$, are likely to impact starting and unstarting. Consequently, artificial mechanisms for boundary layer control have been studied, like boundary layer bleeding [18, 24]. However, these mechanisms are not part of this study.
Finally, previous studies have found, that the starting behavior is dependent on the speed of the variation of flow parameters (see ch. 1.4).

Kantrowitz Plot

As depicted in the prior subsection 1.2.4, the main parameters that define whether an intake starts or unstarts are the Mach number M_{cl} at the entry plane of internal flow A_{cl}, the internal contraction ratio CR_{i} and the back pressure. Kantrowitz and Donaldson [20] derived an upper limit for self-starting that relates M_{cl} and CR_{i}, which is often referred to as Kantrowitz criterion. An intake is called self-starting, if it starts for a given Mach number without the use of bleed flow or variable geometry [35]. The derivation of the Kantrowitz criterion is based on the assumption, that, during unstarted mode, a normal shock exists upstream of the intake that is swallowed by the intake if the flow is accelerated to $M = 1$ at the throat area A_{th}. For this acceleration, the isentropic one-dimensional flow relations are applied, which finally

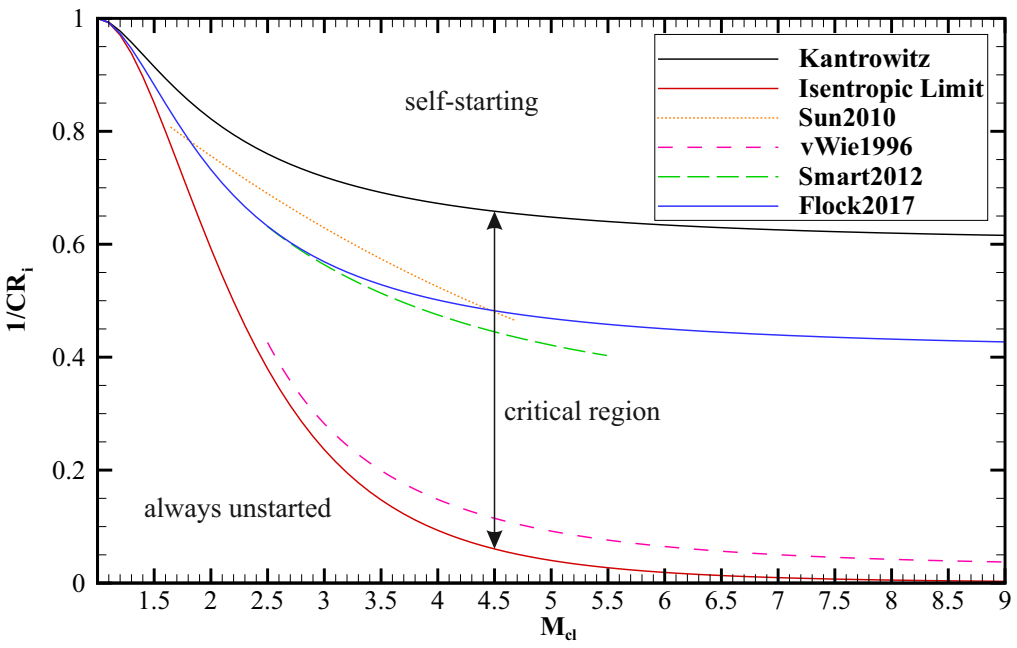

Figure 1.6: Kantrowitz plot with a selection of criteria for self-starting

leads to:

$$CR_{\mathrm{Kantr}} = \frac{A_{\mathrm{cl}}}{A_{\mathrm{th}}} = \frac{(\gamma+1)M_{\mathrm{cl}}^2}{(\gamma-1)M_{\mathrm{cl}}^2+2}^{0.5} \frac{(\gamma+1)M_{\mathrm{cl}}^2}{2\gamma M_{\mathrm{cl}}^2-(\gamma-1)}^{\frac{1}{\gamma-1}} \tag{1.15}$$

Being derived as an upper limit for self-starting, the Kantrowitz criterion turned out to be a conservative estimate [40]. However, it correctly predicts the qualitative relation between CR_{i} and M_{cl}. Therefore, it is a helpful tool to analyze the self-starting capability of intakes.

The maximum possible contraction ratio for given M_{cl}, for which started flow can exist, is determined by isentropic compression (Eq. 1.2) and is therefore called isentropic limit:

$$CR_{\mathrm{isentr}} = \frac{A_{\mathrm{cl}}}{A_{\mathrm{th}}} = \frac{1}{M_{\mathrm{cl}}}\left[\frac{2}{\gamma-1}\left(1+\frac{\gamma-1}{2}M_{\mathrm{cl}}^2\right)\right]^{\frac{\gamma+1}{2(\gamma-1)}} \tag{1.16}$$

In figure 1.6, the isentropic limit is plotted alongside the Kantrowitz criterion with $1/CR_{\mathrm{i}}$ on the y-axis and M_{cl} on the x-axis, resulting in the so-called Kantrowitz plot. The two limits divide the plot into three characteristic regions: For larger contraction ratios than the isentropic limit an intake cannot operate in a started mode. For lower contraction ratios than the Kantrowitz limit, intakes are self-starting according to the Kantrowitz criterion, but once started, they can be operated beyond the criterion [20]. The region between these limits is referred to as critical region, since intakes can operate in the started mode but also in the unstarted mode under certain conditions. Within this region it is necessary to perform further analysis in order to predict the flow state. As the Kantrowitz criterion limit turned out to be conservative, also configurations in the critical region can be self-starting.

In order predict self-starting capabilities more accurately, several empirical or semi-empirical limits have been proposed amongst others by Sun [35], Smart [32] and most recently Flock [12, 13]. These limits are plotted into the Kantrowitz plot in figure 1.6.

In analogy to the derivation of the Kantrowitz criterion, Flock [12, 13] derived an alternative semi-empirical criterion for self-starting by assuming a strong oblique instead of a normal shock

$$CR_{\mathrm{Flock,semi-emp}} = CR_{\mathrm{isentr}} \cdot \Pi_{\mathrm{t}} \tag{1.17}$$

where Π_{t} is the total pressure ratio within a presumed oblique shock with the shock angle $\beta_{\max}$ that corresponds to the highest possible deflection angle $\theta_{\max}$ for a given M before the shock detaches. $\theta_{\max}$ can be obtained by solving equation 1.4. For easier usage and in order to implement an option to adapt the criterion, Flock proposed an empirical relation:

$$CR_{\mathrm{Flock,emp}} = \frac{CR_{\mathrm{Kantr}}}{C_F + CR_{\mathrm{Kantr}}(1 - C_F)} \tag{1.18}$$

With the parameter C_F, the criterion can be adjusted: For $C_F = 1$ the criterion merges into the Kantrowitz criterion and for $C_F = 1.5$ it resembles the semi-empirical criterion described above [12].

Sun and Zhang [35] and Smart [32] proposed empirical limits for self-starting by polynomial fitting of experimental data. Both limits are within the critical region and therefore predict self-starting for higher CR_{i}. However, Smart states, that 2D-intakes are accurately approximated by the Kantrowitz criterion. The limit of Sun and Zhang is valid for the range of $1.65 \leq M_{\mathrm{cl}} \leq 4.68$:

$$CR_{\mathrm{Sun}} = 0.933 + \frac{1}{6.87} M_{\mathrm{cl}} + \frac{1}{40.9} M_{\mathrm{cl}}^2 \tag{1.19}$$

Van Wie, Kwok and Walsh [41] introduced a quadratic fit through experimental data to predict unstart in the region of $2.5 \leq M_{\mathrm{cl}} \leq 10$:

$$\frac{1}{CR_{\mathrm{vWie}}} = 0.05 - \frac{0.52}{M_{\mathrm{cl}}} + \frac{3.65}{M_{\mathrm{cl}}} \tag{1.20}$$

This limit accounts for viscous losses and the effects of shock waves, which reduce the maximum internal contraction ratio compared to the isentropic limit.

1.3 Numerical Fundamentals

1.3.1 Turbulence Modeling

Turbulence are irregular flow motions that are superimposed to the mean flow. Turbulence induces increased momentum, mass and energy transfer and thereby influences the mean flow. These motions reach down to small length scales [43]. Resolving all these length scales numerically is called Direct Numerical Simulation (DNS) and requires computational resources that are impractical for most applications [29, pp. 134f.]. Therefore, Large Eddy Simulations (LES) model the small turbulent length scales and Reynolds-Averaged Navier-Stokes Simulations (RANS) model the complete turbulent flow scales. The current industrial standard is RANS-modelling [29, p.138].

For the RANS equations, the flow is divided into the mean flow velocity c_i and the fluctuating component c_i' (respectively p and p'), which is referred to as *Reynolds Decomposition*. By introducing this decomposition into the Navier-Stokes equations and subsequent time averaging, the RANS equations are obtained [27]:

$$\frac{\partial \overline{c_i}}{\partial t} + \overline{c_j}\frac{\partial \overline{c_i}}{\partial x_j} = -\frac{1}{\rho}\frac{\partial \overline{p}}{\partial x_i} + \nu\frac{\partial^2 \overline{c_i}}{\partial \overline{x_j^2}} - \underbrace{\frac{\partial \overline{c_i' c_j'}}{\partial x_j}}_{\text{add. term}} \tag{1.21}$$

The equation system has the same form as the Navier stokes equations but contains an additional term that introduces 6 additional unknowns. The new term can be interpreted as a stress tensor (Reynolds Stress Tensor $\tau_{\mathrm{tu},ij} = -\rho\overline{c_i' c_j'}$) and needs to be modeled in order to solve the equations. This problem is referred to as closure problem. Most approaches to solve the closure problem make use of the Boussinesq approximation, which assumes the turbulent shear stresses to be proportional to the mean velocity gradients and introduces the turbulent viscosity ν_{tu} as a scalar and isotropic parameter:

$$\tau_{\mathrm{tu},ij} = \rho\nu_{\mathrm{tu}}\left(\frac{\partial \overline{c_i}}{\partial x_j} + \frac{\partial \overline{c_j}}{\partial x_i}\right) - \frac{2}{3}\rho k\delta_{ij} \tag{1.22}$$

where $\delta_{ij} = 1$ if $i = j$ and $\delta_{ij} = 0$ if $i \neq j$ and k is the mean specific turbulence kinetic energy $k = \frac{1}{2}\overline{c_i' c_i'}$ (hereinafter "turbulence kinetic energy").

Spalart-Allmaras Turbulence Model

The Spalart-Allmaras model is a one-equation model for solving the closure problem of the RANS equations. It solves an empirically derived transport equation directly for the turbulent viscosity ν_{tu} and uses the wall distance as parameter. The Spalart-Allmaras model adds only one additional equation to the RANS equations and thus requires relatively little extra computational effort [33]. The model was developed and optimized for airfoil flows and is the most widely used one-equation model [29, p.146f.].

k-ε Turbulence Model

The k-ε turbulence model is a two-equation model that solves transport equations for the turbulence kinetic energy k and the turbulent rate of dissipation ε. The transport equation is obtained by applying the Reynolds decomposition to the NS-equations and subtracting the RANS-equations from these equations. Subsequent tensor contraction with the velocity vector c_j and averaging of the resulting equation leads to [43, p. 89]:

$$\frac{\partial k}{\partial t} + \overline{c_j}\frac{\partial k}{\partial x_j} = \frac{\partial}{\partial x_j}\frac{\nu_t}{\sigma_k}\frac{\partial k}{\partial x_j} - \overline{c_i' c_j'}\frac{\partial \overline{c_i}}{\partial x_j} - \varepsilon \tag{1.23}$$

The k-ε model produces good results in the free flow, but exhibits weaknesses close to viscous walls [29, p. 146].

k-ω Turbulence Model

The k-ω turbulence model is similar to the k-ε model, but solves a transport equation for dissipation per unit turbulent kinetic energy ω:

$$\omega = \frac{\varepsilon}{k} \tag{1.24}$$

instead of ε. Originally introduced by Kolmogorov in 1942, the presently most frequently used formulation of the transport equation for ω is given by Wilcox [42]:

$$\frac{\partial \omega}{\partial t} + \overline{c_j}\frac{\partial \omega}{\partial x_j} = C_{\omega 1}\frac{\omega}{k}\left(-\overline{c_i c_j}\frac{\partial \overline{c_i}}{\partial x_j}\right) + \frac{\partial}{\partial x_j}\left(\frac{\nu_t}{C_{\omega 3}}\frac{\partial \omega}{\partial x_j}\right) - C_{\omega 2}\omega^2 \tag{1.25}$$

$C_{\omega 1}$, $C_{\omega 2}$ and $C_{\omega 3}$ are constants that are usually determined by DNS for representative cases.

In contrast to the k-ε-model, the k-ω-model obtains good results in viscosity dominated areas like in the proximity of the wall, but encounters deficiencies in the free flow [29, p. 146].

Shear-Stress Transport Turbulence Model

The Shear-Stress Transport (SST) model combines the k-ε- and k-ω-model by introducing a blending function. Thereby, it combines the good performance of k-ω in the viscosity dominated flow in the proximity of the wall and the advantages of k-ε in the free flow [29, p. 146]. Additionally, the SST-model utilizes the Bradshaw hypothesis to relate the turbulent shear stress τ_{tu} to the turbulent kinetic energy k in the logarithmic part of two-dimensional boundary layers:

$$\overline{u'v'} = \rho a_1 k \tag{1.26}$$

An additional blending function is used to restrict the influence of the Bradshaw hypothesis to the proximity of the wall. Menter argues that the usage of the Bradshaw hypothesis introduces a model of the transport of the turbulent shear stresses thus giving the SST-model its name [23].

1.3.2 Mesh

For CFD, the flow field is discretized into a numerical mesh, consisting of a finite number of elements. Computational meshes can be divided into structured and unstructured meshes. Whereas structured meshes have superior computational behavior, unstructured meshes can be easily refined in regions of interest or high gradients [22].

Local refinement is necessary to reduce the truncation error and to have enough cell points in regions of high gradients to be able to resolve the physics of the flow correctly [6]. A common region of refinement is a set of prism layers at viscous walls – often called boundary layer inflation (BLI). The prisms within the boundary layer inflation have a high stretching in wall parallel direction and are fine in wall normal direction. Therefore, the high gradients in wall normal direction can be resolved without unnecessary refinement in wall parallel direction. Since boundary layer thickness and its gradients are to be resolved by the mesh, the non-dimension wall distance y^+ is defined:

$$y^+ = \frac{\sqrt{\tau_{\mathrm{w}}/\rho}}{\nu} y \tag{1.27}$$

with τ_{w} being the wall shear stress and ν the kinematic viscosity of the fluid [39, pp. 362ff.; 28, pp. 546f.]. For RANS-methods $y^+ \leq 1$ should hold to ensure sufficiently precise capturing of boundary layer characteristics [2].

1.3.3 CFL Number

The Courant-Friedrich-Levy (CFL) number is a stability parameter for explicit schemes, that relates the ratio of step size in time and space to the characteristic velocity of propagation:

$$CFL = \left.\frac{\partial x}{\partial t}\right|_c \frac{\Delta t}{\Delta x} \tag{1.28}$$

In classical stability analysis, the CFL-condition is applied to calculate the maximum stable Δt. It states, that the numerical domain must fully include the physical domain for a stable simulation of hyperbolic equations [6].

1.3.4 Marching Scheme

Central schemes usually exhibit problems in super- and hypersonic flows with strong shocks: They have slow convergence and are inaccurate in the shock regions. Upwind schemes are more precise and stable in the proximity of shocks but more inaccurate in other flow regions. Upwind schemes contain an "inherent physical damping" by taking into account that disturbances propagate along the characteristics [2, pp. 36ff.; 22, p. 84].

1.4 Current Scientific Knowledge

The process of starting and unstarting has been studied for decades with analytical, experimental and lately also numerical methods. However, the process is still not fully understood and thus is still subject of research.

The existence of a hysteresis between started and unstarted mode has been proven by experimental studies. Stephen et al. [34] experimentally investigated the influence of varied angle of attack and sideslip angle on a three-dimensional intake for $3 \leq M_\infty \leq 4.3$. They showed restarting of the intake for sideslip angles in both directions and for angles of attack that decreased the relative ramp angle of the most upstream ramp region. Furthermore, they demonstrated that a hysteresis is present for starting and unstarting with angle of attack. Once started, the flow remained in started mode if the flow angle was rotated back into neutral position. Further rotation in the direction of increased relative angles of the upstream ramp eventually caused unstart. If the rotation was then reversed, the intake remained unstarted until reaching the critical angle for starting. Flock [12] proved, that a hysteresis between started and unstarted mode also exists for varied internal contraction ratio CR_i. He conducted wind Tunnel tests on a three-dimensional intake with traversable cowl. Flock observed, that once the intake was started, CR_i could not be unstarted by increased contraction ratio within the traversation limits of the cowl.

In the past years, many different techniques to support intake starting have been proposed and investigated. Many of these techniques make use of unsteady phenomena such as diaphragm rupture, which was studied by Ogawa et al. [25], Tahir et al. [36] and Timofeev et al. [38]. The diaphragm therefore either covers the intake or the nozzle of the engine and thus prohibits internal flow. Whereas Timofeev and Tahir applied inviscid Euler equations, Ogawa performed viscous simulations with k-ε turbulence modelling. All approaches made use of transient simulations and were able to achieve starting after the diaphragm rupture. One problem of starting with diaphragm rupture is that unstarted intakes cannot be restarted with this approach. This shortcoming can be overcome by substituting the diaphragm with movable or rotating doors according to studies of Donde et al. [11], Grainger et al. [14], Jacobsen et al. [18] and Ogawa et al. [25]. Therefore, the doors initially shield the intake and are rapidly opened to induce starting. All of the above stated approaches to simulate starting via rapidly opening doors used

viscous simulations with RANS-modeling and transient simulations. Grainger et al. additionally compared the results obtained by a fully three-dimensional to the results of a two-dimensional axisymmetric simulation of the same intake. He concluded, that both approaches agreed well. The most significant problem of unsteady starting techniques are the high mechanical loads on the intake [14]. The possibility of intake starting via bleed flow has been studied numerically by Jacobsen et al. [18] and Nahafiyazdi et al. [24], among others. Jain and Mittal [19] and Karl [21] analyzed intake unstarting due to backpressure. Jain and Mittal applied unsteady Euler simulations to a two-dimensional intake with mixed internal and external compression and a divergent region after the throat at $M_\infty = 3$. Additionally, they demonstrated the relevance of the curvature around the throat for intake unstarting. Karl performed unsteady simulations with several RANS turbulence models of a two-dimensional intake with bleed flow. He applied backpressure according to additional simulations in the combustion chamber. Karl concludes, that turbulence models had a strong effect on the complex combustor flow field and that the Menter SST model performed best in reproducing experimental results. All of these numerical studies have in common, that they perform transient simulations to capture the behavior of starting and unstarting.

2 Methodology

2.1 Procedure

2.1.1 Quasi-Steady Approach

The goal of this work is to analyze the unsteady transition between started and unstarted mode of intakes by applying a novel quasi-steady approach. This approach significantly reduces computational costs compared to unsteady calculation of the flow. In order to guarantee quasi-steady conditions, parameters have to be varied with sufficiently low step size, since unsteady effects can affect starting and unstarting (see ch. 1.4). Since the approach is not time-accurate, unsteady starting processes, such as diaphragm rupture, cannot be analyzed. Within this work, starting and unstarting due to varied free stream Mach number M_∞ or angle of attack α is analyzed.

To analyze starting and unstarting with this approach, a set of steady RANS simulations is performed. Within the first step, the initial solution is calculated. For the next step, the independent parameter (M_∞ or α) is varied slightly (e.g. increased), and a subsequent RANS simulation is started with the previous steady state solution as initial condition.

Figure 2.1 shows a sample analysis with M_∞ as independent parameter. The analysis consists of multiple "steps" (dashed ellipse) between which M_∞ is varied incrementally. Each step consists of two individual steady simulations, which shall be called "runs" and are depicted as squares. Firstly, an initial run is performed with a reduced CFL-number of $CFL = 0.6$ to allow for stable initialization. The initial run is performed for 10,000 iterations, if the convergence criterion of $Res_\rho = 10^{-12}$ is not reached. Secondly, a final run with $CFL = 1.5$ is performed to accelerate convergence with a maximum of 80,000 iterations. For each run, the steady state solution of the previous run is prescribed as initial condition. For the initial run of the first step, no initial solution is available, so the complete numerical domain is initialized with the reference parameters (i.e. $M = M_\infty$). For the presented sample analysis, the free stream Mach number M_∞ of the first step is bigger than the critical free stream Mach number $M_{\infty,\mathrm{unstart}}$, for which the examined intake unstarts. Therefore, the first step will result in a started flow field – regardless of whether the critical Mach number for starting $M_{\infty,\mathrm{start}}$ is exceeded, since the initial condition of $M = M_\infty$ is closer to started than to unstarted mode. Note, that both $M_{\infty,\mathrm{start}}$ and $M_{\infty,\mathrm{unstart}}$ are unknown a priori and thus have to be estimated. After the final run of the first step is sufficiently converged, the simulation is stopped and its solution files are saved, which marks the end of this step. Subsequently, the next step is started with the solution of the first step as initial condition and a slightly decreased M_∞. In this case, the new M_∞ is smaller than $M_{\infty,\mathrm{unstart}}$ and thus the simulated flow field will unstart within the second step. If M_∞ is increased for subsequent steps, the simulated flow will not restart until $M_\infty > M_{\infty,\mathrm{start}}$, with $M_{\infty,\mathrm{start}} > M_{\infty,\mathrm{unstart}}$ (see ch. 1.2.4) and thus a hysteresis establishes. The complete set of steps shall be called "series".

Each run consists of preprocessing and the actual simulation. During the preprocessing of the initial run of the first step, the mesh is divided into the specified number of domains for parallel computation. Additionally, parameters that are specified in the BMAP-file (see ch. 2.3.1) are updated during preprocessing.

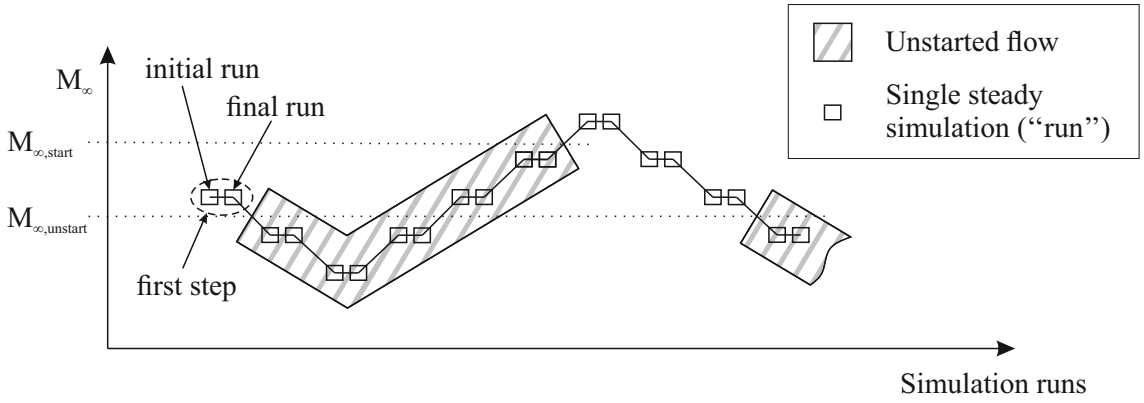

Figure 2.1: Schematical quasi-steady approach with established hysteresis

For conditions where hysteresis is present, the flow mode (started or unstarted) is dependent on the history of the flow. Besides this behavior, no further dependence of the history of the flow field on the converged steady state solutions have been found. Therefore, starting and unstarting could be analyzed independently. Furthermore, subsequent refinement in critical regions was possible. However, the step size between two subsequent runs had to be limited to ensure numerical stability and quasi-steady behavior.

2.1.2 Adaptation of Dependent Parameters

Two different modes have been developed to adjust the prescribed dependent variables p_∞, T_∞, and T_w to the free stream Mach number M_∞: Flight mode and wind tunnel mode (see table 2.1).

The wind tunnel mode was implemented to achieve similarity (compare ch. 1.2.3) with experiments that were performed in the TMK-facility and will be discussed in chapter 2.4. For this purpose, the total temperature is set constant to $T_\mathrm{t} = 300$ K, if not otherwise stated. Consequently, the static temperature of the free stream T_∞ is:

$$T_\infty = \frac{T_\mathrm{t}}{1 + M_\infty^2 \frac{\gamma-1}{2}} \tag{2.1}$$

The static pressure of the free stream p_∞ is calculated with:

$$p_\infty = \frac{2q_\infty}{\gamma M_\infty^2} \tag{2.2}$$

for a constant dynamic pressure that is set to $q = 1$ bar unless otherwise stated. For wind tunnel mode, the wall temperature was set to $T_\mathrm{w} = 300$ K. Consequently, $T_\mathrm{w} = T_\mathrm{t}$, which approximately corresponds to adiabatic conditions.

Within wind tunnel mode, the unit Reynolds number Re_u varies slightly with M_∞ as depicted in figure 2.2. To calculate the unit Reynolds numbers, Sutherland's law, which is valid except for high temperature flows [5, p.647], was applied to calculate μ_∞ in dependence of T_∞:

$$\mu_\infty = \mu_\mathrm{r} \left(\frac{T}{T_\mathrm{r}}\right)^{\frac{3}{2}} \frac{T_\mathrm{r} + C_\mu}{T_\infty + C_\mu} \tag{2.3}$$

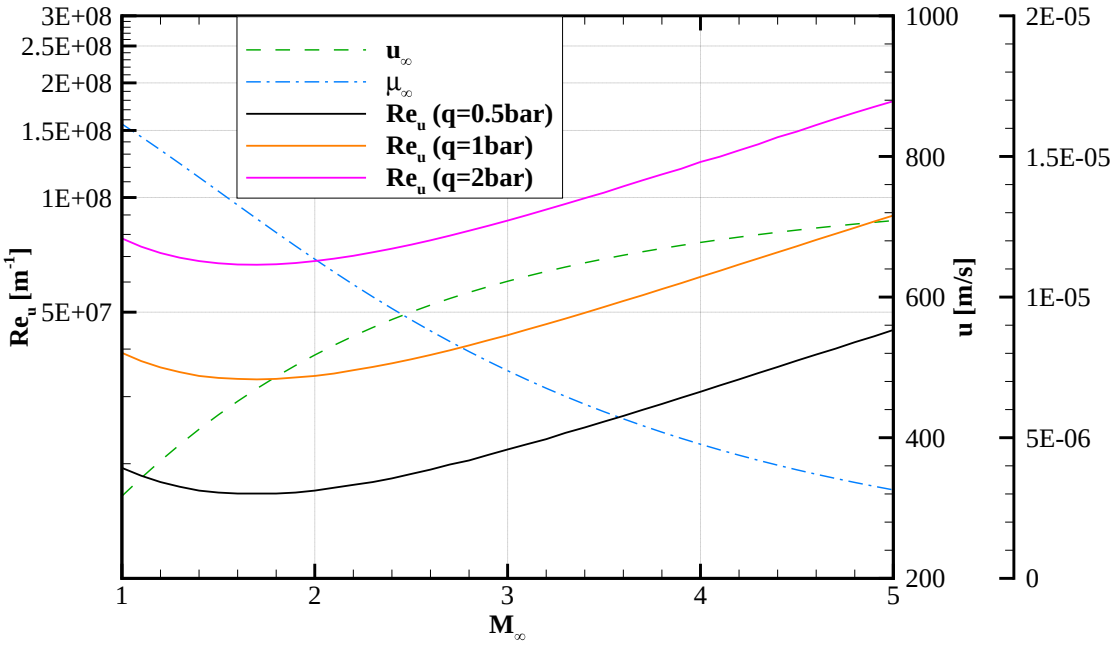

Figure 2.2: Dependence of free stream parameters on M_∞ for wind tunnel mode

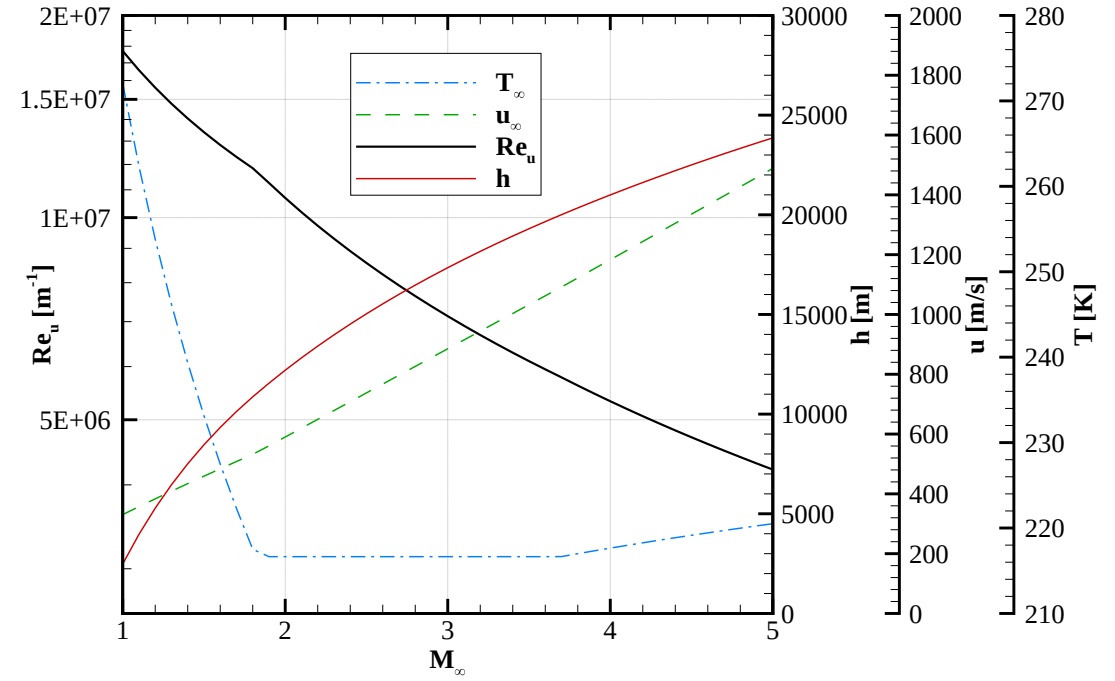

Figure 2.3: Dependence of free stream parameters on M_∞ for flight mode with $q = 0.524$ bar

Mode	input
Flight	q_∞, M_∞, $T_\mathrm{w}/T_\mathrm{t}$
Wind Tunnel	q_∞, M_∞, T_t

Table 2.1: Boundary condition Modes

For wind tunnel mode, the unit Reynolds number Re_u can be expressed as a function of q_∞, T_∞ and u_∞, if the dynamic viscosity μ_∞ is only dependent on T_∞:

$$Re_\mathrm{u} = \left.\frac{\rho u}{\mu}\right|_\infty = \left.\frac{2q}{u\mu}\right|_\infty = 2q_\infty \cdot f(u_\infty, T_\infty) \tag{2.4}$$

Since in wind tunnel mode, T_∞ and u_∞ are only dependent on the total temperature T_t and the free stream Mach number M_∞, and T_t is constant, the Reynolds number is proportional to the dynamic pressure for constant M_∞. Thus, a direct relationship between q_∞ and Re_u exists, consequently a doubled value of q_∞ results in a doubled Reynolds number Re_u.

The flight mode simulates a trajectory with $q = \mathrm{const.}$ within earth's atmosphere, which is a common basis for hypersonic trajectory development [15, p. 38]. The atmosphere was modeled with the U.S. Standard Atmosphere, which is consistent with the International Standard Atmosphere (ISA) up to 50km [1]. Within flight mode, p_∞ and T_∞ are prescribed as the ambient values at the corresponding altitude according to the U.S. Standard Atmosphere. The corresponding altitude is determined by the ambient pressure, that is necessary to produce a specified dynamic pressure q_∞ for a given M_∞ as in equation 2.2. The wall temperature was set to a specified ratio $1/C_\mathrm{w}$ of the total temperature:

$$T_\mathrm{w} = \frac{T_\mathrm{t}}{C_\mathrm{w}} \tag{2.5}$$

For flight in the atmosphere at constant dynamic pressure, the vehicle has to continuously ascend during acceleration as depicted in figure 2.3. Consequently, the ambient temperature drops significantly until reaching the tropopause at $h = 11.000\ m$. The unit Reynolds number Re_u decreases continuously during acceleration. The rate of decrease is accelerated once the Tropopause is reached, where the ambient temperature is modeled to be constant.

The ratio of specific heats γ and the Prandtl number Pr_∞ are both functions of the gas and are treated as constant for both modes ($\gamma = 1.4$, $Pr_\infty = 0.72$). Furthermore, the flow is assumed to be chemically non-reactive. These assumptions are valid for a constant composition of the ambient gas and gas temperatures below 600 K [3, 40]. For the considered wind tunnel conditions, flow temperatures are below 300 K, and thus these assumptions are valid.

Within flight-mode, temperatures partially exceed 600 K. Consequently, γ and Pr_∞ could vary in real flows during flight, which should be kept in mind. However, Wie [40] states, that for an intake at $M_\infty = 15$, $q = 47880$ Pa $= \mathrm{const.}$ and $\Pi_\mathrm{s} = 250$, the optimal compression ratio differs 13% between ideal and real gas solutions. In the current work, intakes with significantly lower Π_s and M_∞ are studied, thus also the resulting error for flight mode is assumed to be significantly lower.

2.1.3 Automation of Simulations

To reduce the amount of manual input and to make efficient use of the computational resources, an automation script named *HYSIF* (HYsteresis of Supersonic Intake Flows) was developed using *python*. The script edits the input-file for the flow solver TAU (will be discussed in ch. 2.3.1) and creates boundary-mapping-files (BMAP) for every individual run according to the specified parameters. The independent parameters α and M_∞ are analyzed separately, thus only one is varied within one series. The complete set of the independent parameter for the series is specified explicitly as a list, which allows for variable step size. This enables sufficient accuracy in the transitional regions while reducing computational costs in less critical regions.

2.1.4 Post processing

In order to analyze and compare complete hystereses, average values were extracted by automatizing *extract1D.exe* written by Dr. Andreas Flock. *Extract1D.exe* analyzes plane cuts extracted from more-dimensional solutions and returns weighted averages. The differences between these averaging methods are especially relevant if the mean flow direction is not uniform. Strong non-uniformity is present in regions with flow separation, or if a shock intersects the averaging plane. While area and mass-rated averages are both sensitive to the local height of the separation bubble, mass-flow-rated averages are less dependent on this influence [7]. Since the location (and therefore the local height) of the separation bubble is often unsteady, mass-flow-rated averages are better suited to describe the flow field. Therefore, mass-flow-rated averages will be used in the following, unless otherwise stated.

For this study, *extract1D.exe* was automatized as *AEX1D* (Automatic EXtract1D). Additionally, *AEX1D* calculates the Mass capture ratio MCR by using the nominal mass flow through the capture area A_0, $\dot{m}_0$:

$$MCR = \frac{\dot{m}_{\mathrm{extract1D}}}{M_\infty A_0 p_\infty \sqrt{\frac{\gamma}{RT_\infty}}}, \tag{2.6}$$

where p_∞, T_∞, M_∞ are the reference parameters extracted from the TAU-input-file (see 2.3.1).

2.2 Analyzed Geometries

In this study, two-dimensional ramp intakes and an axisymmetric intake with movable centerbody were analyzed. The axisymmetric model served as validation case. The x-coordinate was defined to start at the tip of the cone or the first ramp for the axisymmetric and two-dimensional case, respectively. All areas were defined as perpendicular to the x-direction.

2.2.1 Two-Dimensional Ramp Intakes

The generic two-dimensional intakes consist of a finite number of ramps, a cowl and an isolator that is oriented in flow direction. They are designed for a certain Mach number $M_{\infty,\mathrm{DP}}$. For the design process, started flow is assumed and the analytical shock relations are applied. Consequently, viscous effects are neglected (see ch. 1.2.2). The design process has 3 constraints in the case of $M_\infty = M_{\infty,\mathrm{DP}}$ and inviscid flow (depicted in figure 2.4):

i) Every ramp shock impinges at the cowl tip

ii) Every ramp has equal shock angle relative to its upstream region

iii) The cowl shock impinges at the junction of the last ramp and the isolator and thus is not reflected

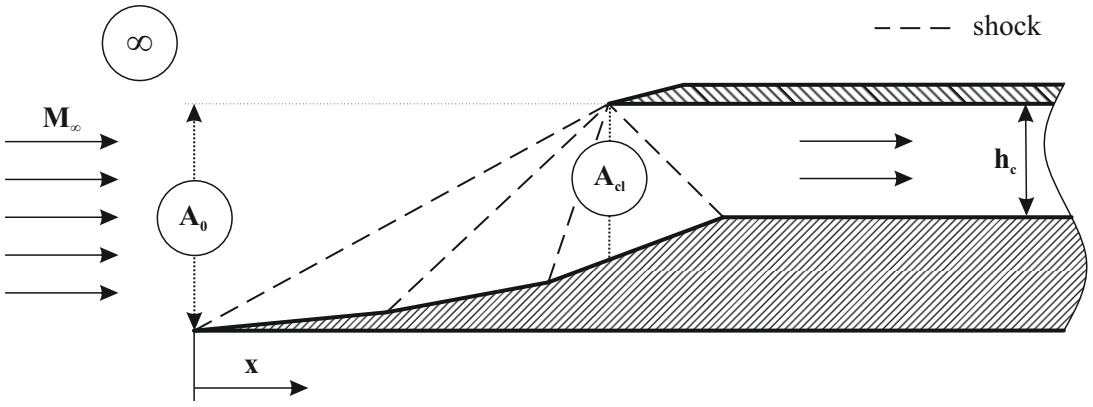

Figure 2.4: Simplified 2D-intake with flow at design conditions

These constraints lead to high efficiency: Firstly, the shock-on-lip configuration leads to $MCR = 1$ and thus maximum mass flow and consequently potentially high thrust. Secondly, equal strength of ramp shocks leads to maximum pressure recovery in 2D-Ramjet intakes, which is known as Oswatitsch-criterion [26]. This criterion was proven to be a good approximation also for two-dimensional Scramjet intakes [30].

If the number of ramps n_{ramps}, the height of the combustor h_{cc}, the design Mach number $M_{\infty,\mathrm{DP}}$ and the design static pressure ratio $\Pi_{\mathrm{st,DP}}$ (inviscid) are specified, the intake-geometry can be calculated by using the shock relations (see ch. 1.2.2). This task was performed by an existing tool *SING2D.exe* (Supersonic INtake Design 2D) written by Dr. Andreas Flock, which was further automated in order to create multiple geometries.

In this work, intakes with different n_{ramps}, $M_{\infty,\mathrm{DP}}$ and $\Pi_{\mathrm{st,DP}}$ have been studied. The combustion chamber's height h_{cc} was kept constant at $h_{\mathrm{cc}} = 40\ \mathrm{mm}$ to allow for comparison with studies within the Research Training Group 1095 [17]. In figure 2.5 different design points of two-dimensional intakes are plotted into the Kantrowitz plot. Additionally, the tendencies of increasing n_{ramps}, $M_{\infty,\mathrm{DP}}$ and $\Pi_{\mathrm{st,DP}}$ are depicted in order to visualize their general impact on self-startability. The most significant effect, is that for the design of intakes with increased design static pressure ratios $\Pi_{\mathrm{s,DP}}$, increased (internal) contraction ratios CR_{i} are required and lead to increased deceleration of the flow to lower $M_{\mathrm{cl,DP}}$, which both reduces the tendency to self-start. Additionally, a higher design Mach number $M_{\infty,\mathrm{DP}}$ shifts the design point to higher cowl Mach numbers $M_{\mathrm{cl,DP}}$, which translates to a shift to the right in the Kantrowitz plot. Therefore, intakes with bigger design Mach number $M_{\infty,\mathrm{DP}}$ are more likely to be self-starting for their respective design Mach number. Finally, more ramps lead to less shock losses and thus produce bigger $M_{\mathrm{cl,DP}}$ for inviscid flows. However, the internal contraction ratio is slightly increased if more ramps are used, which approximately cancels the increase in $M_{\mathrm{cl,DP}}$. So far, the length of the intake was not taken into account, despite its impact on viscous losses, weight and ease of integration into the vehicle. In order to estimate the feasibility of each intake, their non-dimensional length L/h_{cc} is added. Consequently, increased $\Pi_{\mathrm{st,DP}}$, $M_{\infty,\mathrm{DP}}$ and especially increased number of ramps increase the non-dimensional length and thus increase the difficulty for an efficient integration of the intake into the vehicle.

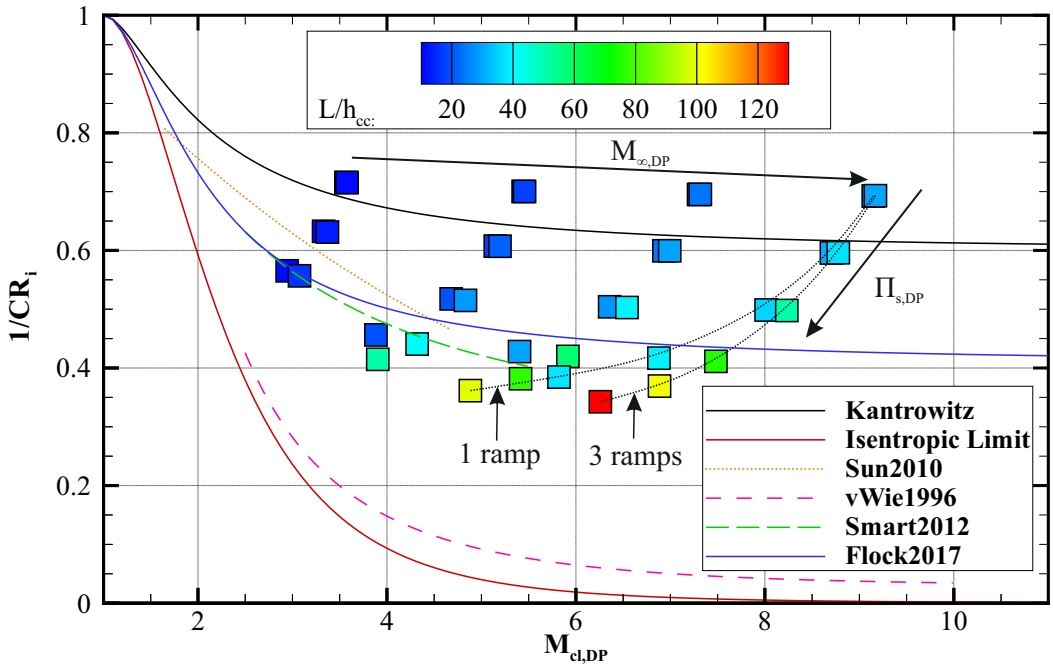

Figure 2.5: Two-dimensional intakes with non-dimensional length plotted alongside startability criteria in Kantrowitz plot

2.2.2 Axisymmetric Intakes

In addition to the two-dimensional geometries, an axisymmetric intake (see fig. 2.6) has been investigated within this study. The same geometry was also experimentally investigated by Dr. Dirk Herrmann at the TMK-facility within the department (see ch. 2.4). Therefore, this case was chosen as validation for the present study. In contrast to the two-dimensional intakes, the cowl tip of the analyzed geometry was designed with a finite radius of $r_{\mathrm{cl}} = 0.5\ \mathrm{mm}$. An additional difference between the axisymmetric intake and the two-dimensional intakes is the divergent region of the internal flow of the axisymmetric intake, that allows for a stable shock position for subsonic combustion (see 1.2.4).

The intake contains a movable cone to adjust the internal contraction ratio CR_{i}, which allows for a broader operational range of Mach numbers. During the wind tunnel tests, the cone was traversed at constant M_∞. Within the numerical studies, cowl positions were constant and therefore analyzed separately. Therefore, each numerical analysis of the axisymmetric intake is denoted by the distance of the ramp tip and the cowl tip x_{c} (see fig. 2.6).

2.3 Numerical Methodology

2.3.1 Flow Solver TAU

TAU is a parallelizable finite volume flow solver for hybrid three-dimensional meshes that is developed by DLR. It follows the finite volume approach, where flow variables are stored on the cell vertices. Either the compressible Euler or the compressible RANS equations can be solved with TAU. [2]

In this study, a central discretization scheme was applied for solving the Euler equations, that achieves second order accuracy. For solving the compressible RANS equations, an upwind scheme (AUSMDV)

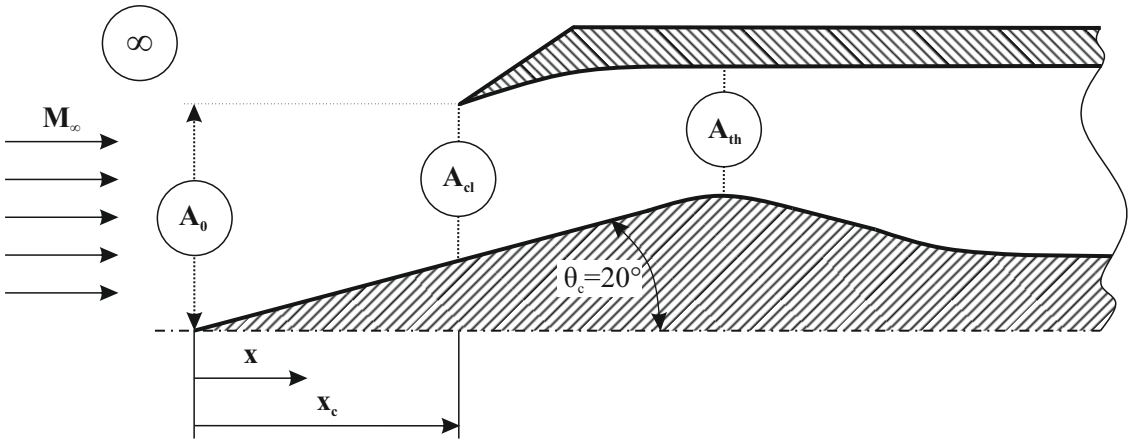

Figure 2.6: Simplified axisymmetric intake

was used to achieve stable simulations. The both upwind fluxes and additional equations were solved with second order accuracy, which proved to be critical for reliable prediction of starting. Furthermore, explicit time-stepping was applied by using a Runge-Kutta relaxation solver with 3 stages.

The simulation parameters such as turbulence model and reference parameters are defined in an input-file. Information about the boundaries are stored in a boundary mapping file (BMAP). Both files can be edited with a conventional text editor or by a script. A characteristic input- and BMAP-file can be found in the Appendix A.

2.3.2 Turbulence Model

Viscosity effects and turbulence have significant impact on starting and unstarting (see ch. 1.2.4). Whereas Euler simulations can only capture the unstarted flow with a normal shock, viscous simulations can also capture unstarted flow with an oblique shock and boundary layer separation. Figure 2.7 shows the different unstarting modes resulting from viscous (top) and Euler simulation (bottom) for a two-dimensional intake at $M_\infty = 4$. The location and size of the separation bubble are strongly affected by turbulence and consequently turbulence modeling [43, p.165].

Within this study, several one- or two-equation turbulence models have been compared regarding their capability to accurately predict the wall-pressure and the starting behavior according to the experiments. The investigation was conducted for the axisymmetric intake, since the experiments (see ch. 2.4) were conducted for this intake. The investigated models have been: The Spalart-Allmaras-model in the O-version (SAO), the Wilcox-k-ω-model (k-ω) and the Menter-SST-model (MenterSST).

As seen in figure 2.8, the k-ω- and SAO-model differ strongly from the Menter-SST-model. Especially the peak at $x \approx 0.22$ m is significantly better approximated by the Menter-SST-model. Regarding the predictions of starting, k-ω- and SAO-model significantly over predict M_∞ for starting if compared to the experiments. The Menter-SST-model agrees better with the experiments, even though it still over predicts M_∞ for starting.

For this study, the Menter SST model was chosen, since it was accurate in capturing the wall pressure of the experiments and also performed best in predicting the starting behavior. Furthermore, it is based on a physical approach rather than a fully-empirical approach (like in the Spalart-Allmaras-model), thus it was better trusted to model the complicated intake flow accurately.

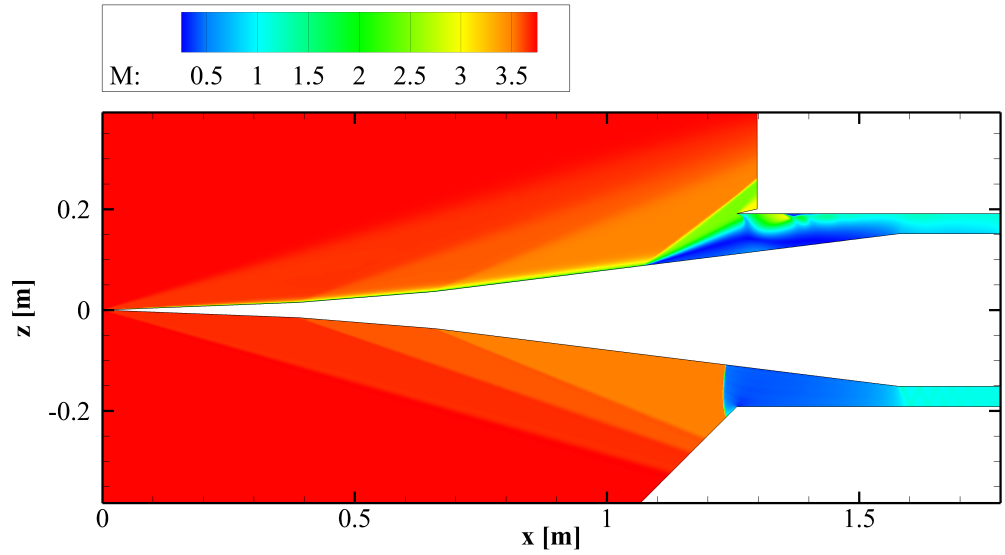

Figure 2.7: Different unstart modes resulting from viscous (top) and inviscid (bottom) simulation for a 2D-intake at $M_\infty = 4$

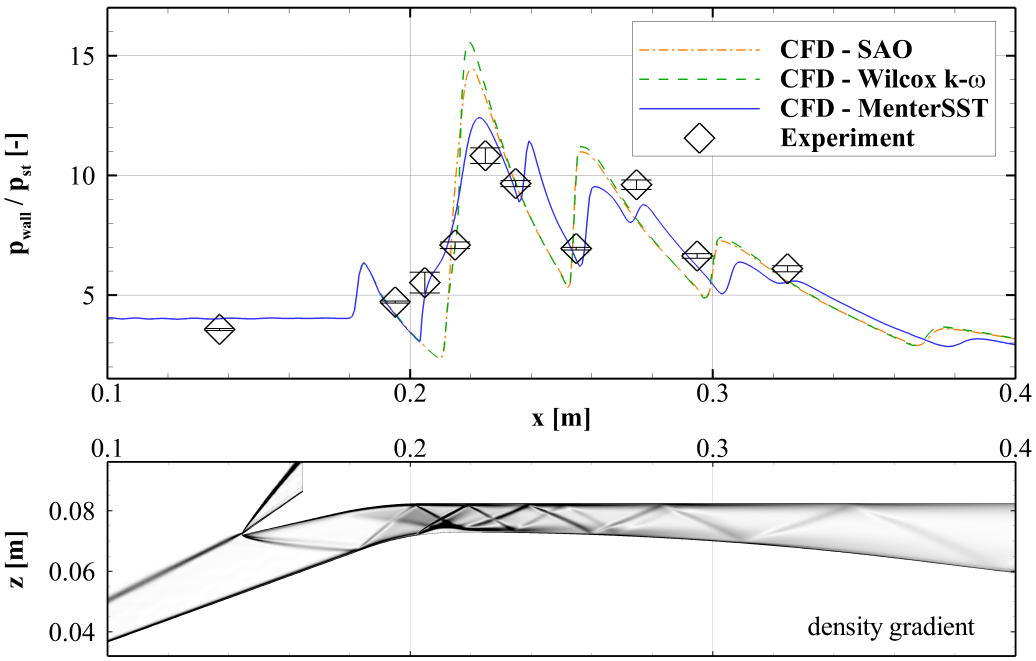

Figure 2.8: Wall-pressure of experiments and calculated by different Turbulence Models for axisymmetric geometry $M_\infty = 4$ and $x_c = 144.6$ mm and numerical Schlieren calculated with Menter-SST-model

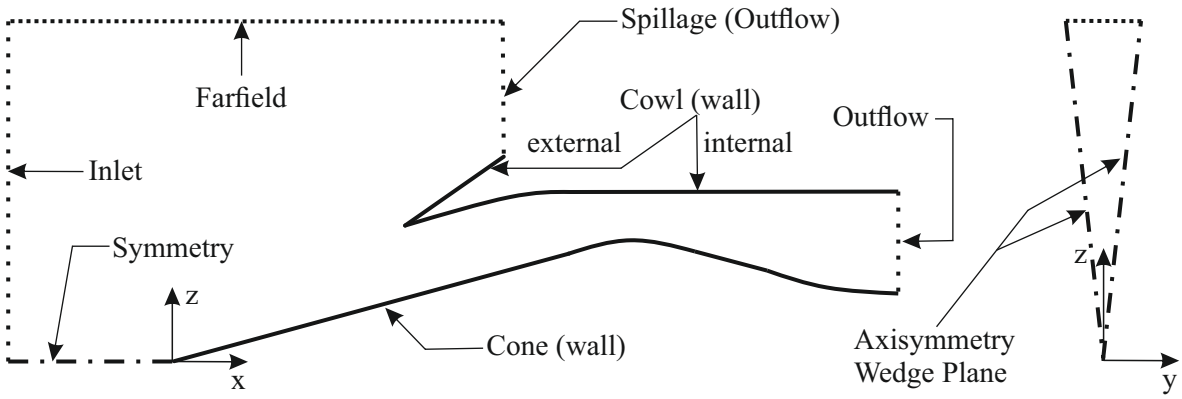

Figure 2.9: Numerical domain of axisymmetric geometry (simplified)

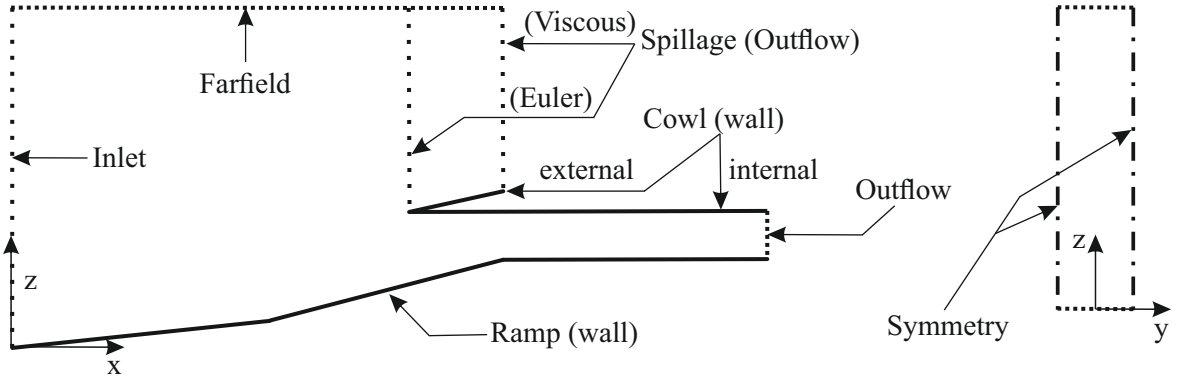

Figure 2.10: Numerical domain of two-dimensional geometry (simplified)

2.3.3 Numerical Domain

The numerical domains for two-dimensional and axisymmetric simulations are similarly structured. As depicted in figures 2.9 and 2.10, the numerical domains are constrained by the supersonic inflow, a central cone or ramp, the outflow area, the cowl, a spillage outflow, and a farfield region. The external part of the cowl is modeled only for viscous simulations. For the two-dimensional intakes, a sharp cowl tip with an external ramp angle of $12°$ was chosen. Furthermore, for the two-dimensional geometries, the symmetry axis is omitted. Thus, the inflow boundary plane and the first ramp directly adjoin each other. For the two-dimensional intakes, it is not necessary for stability to model the free flow upstream of the first ramp, since the turning angle of the first ramp of the analyzed two-dimensional geometries is in general small compared to the axisymmetric intake.

Whereas the depth in y-direction is constant for the two-dimensional intakes, the axisymmetric domain has variable depth corresponding to a wedge with an angle of $1°$. Therefore, the axisymmetric character of the intake is taken into consideration. Via this method, computational costs are reduced significantly in comparison to simulating the complete intake in three dimensions. However, gradients in direction of the angular coordinate can not be observed by this method. Thus, it is not possible to simulate the flow field at angle of attack.

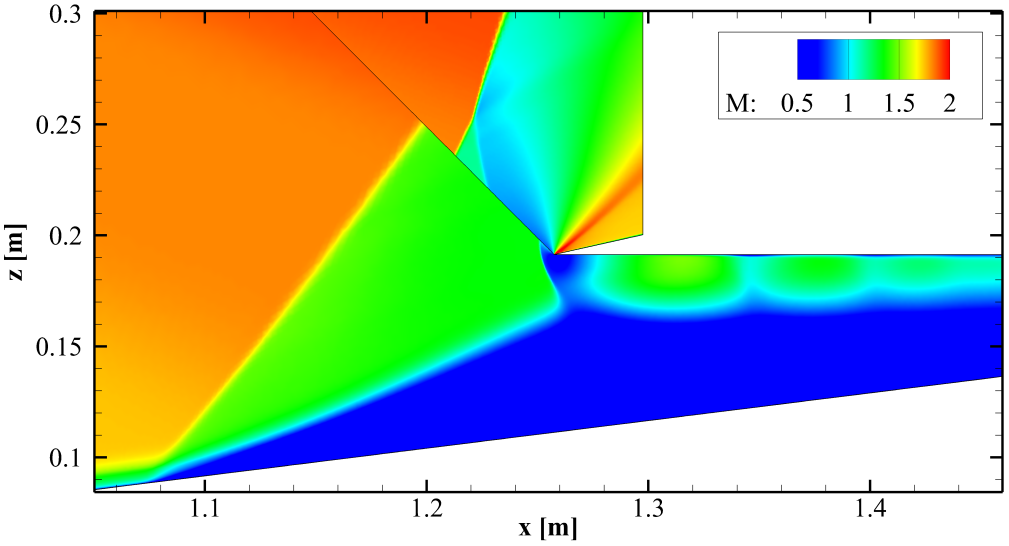

Figure 2.11: Flow fields for two-dimensional intakes with and without modeling of the external cowl area

Boundary Conditions

The prescription of the independent and dependent parameters (see ch. 2.1.2) is same for the axisymmetric and the two-dimensional intakes. The calculated free stream pressure p_∞ and temperature T_∞ are prescribed at the inlet and farfield boundary. Additionally, both are prescribed at spillage and outflow boundaries, which are both defined as exit-pressure outlets. However, for inviscid flows, the prescribed boundary conditions at the outflow boundaries do not affect the upstream flow, if the upstream flow is supersonic. The free stream Mach number M_∞ (and thus u_∞) is prescribed at the inflow and farfield boundaries.

All walls are defined with no-slip boundary condition and the prescribed isothermal wall temperature T_w. Consequently, heat can be exchanged between flow and wall. To avoid adding an additional potential source of errors by using a prediction algorithm for laminar-turbulent transition, the assumption of a fully turbulent boundary layer was chosen for all viscous simulations. Although this is not accurate for the most upstream parts of the ramp, the internal boundary layer however will most probably be turbulent. With the proposed empirical estimation of [8], the transition Reynolds number can be estimated with:

$$\log_{10}(Re_\mathrm{tr}) = 6.421\exp\left[1.209 \cdot 10^{-4} M_\mathrm{e}^{2.641}\right] \tag{2.7}$$

For the axisymmetric intake at wind tunnel conditions and $M_\infty = 4$, and $M_\mathrm{e} \approx 2.8$ (according to CFD-results), this results in:

$$Re_\mathrm{tr} = 10^{6.421\exp\left[1.209\cdot 10^{-4} M_\mathrm{e}^{2.641}\right]} = 2.7 \cdot 10^6 \tag{2.8}$$

$$x_\mathrm{tr} = \frac{\nu}{\sqrt{\gamma R T_\infty} M_\infty} \cdot Re_\mathrm{tr} \approx 4\ \mathrm{mm} \tag{2.9}$$

Considering that the analyzed cone positions are within $130\ \mathrm{mm} \leq x_\mathrm{c} < 148\ \mathrm{mm}$, it seems reasonable to neglect the laminar part.

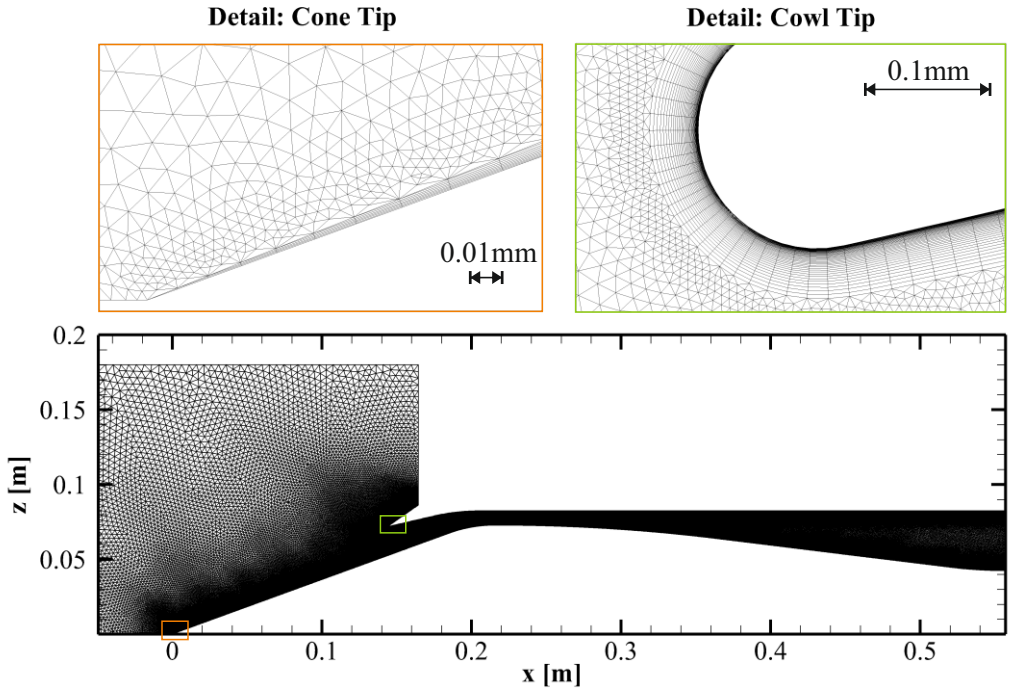

Figure 2.12: Axisymmetric reference Mesh

Mesh Generation

The meshes were created with the hybrid grid generation software *Centaur* as 2D meshes. The input parameters for the generation of the reference mesh of the axisymmetric intake are presented in the Appendix. *Centaur* produces hyb-files that can be transformed into grid-files that are readable by TAU by using the built-in "centaur2tau"-algorithm.

As described in chapter 1.3.2, numerical meshes have to be refined in regions of large gradients. Within supersonic intake flows, the highest gradients occur in the boundary layer and in shocks. It is good practice for steady supersonic simulations to use adaptation tools to automatically refine the mesh in regions of large gradients. However, the objective of this work is to analyze the transition between started and unstarted mode, which significantly differ in the position of shocks and other flow features. Since both modes and their transition have to be captured accurately in one mesh, the usage of automatic refinement would require refinement and derefinement of the mesh between each step. This process is likely to produce regions with poor mesh quality. Furthermore, a mesh generated with this approach would not be adequately refined for shock positions during starting or unstarting. For these reasons, adaptive refinement was omitted and a manually refined mesh was used for all steps instead. Consequently, this mesh has to be sufficiently fine to capture all flow features.

The prism layer is designed to have a maximum y^+-value of 1 at the first layer for every flow condition that is being studied. The tip regions of ramp and cowl mark an exception to this design goal, since the boundary layer height δ approaches zero at the tip. However, the tip regions have been refined both parallel and perpendicular to the wall which can be seen in figure 2.12. In general, the prism layer consists of 55 layers that grow with a stretching ratio of 1.085 perpendicular to the wall.

The prism layer in the region of the ramp tip poses an additional problem: For high Mach numbers, the shock angle β gets smaller so the shock moves closer to the wall. The shock induces a strong gradient

Location of refinement	Refined Elements
A_{cl}	Surface Elements, Triangles
Ramp Tip	Surface Elements, First layer thickness
Cowl Tip	Surface Elements, First layer thickness
Cowl (Internal)	First layer thickness
Cone (Internal)	First layer thickness
Cone (External)	First layer thickness
Throat	Surface & First layer thickness
Cone Tip	Surface (& no. of prism layers)

Table 2.2: Regions of manual refinement (axisymmetric)

that is not parallel to the wall. Since the elements of the prism layer have a large aspect ratio, large gradients which are not perpendicular to the wall are not captured accurately. To avoid this, the number of prism layers is set to zero at the ramp tip and is increased one by one for each prism element in wall-direction until the specified number of prism layers is reached (see fig. 2.12, left). It was shown that this significantly reduces numerical diffusion of the leading edge shock.

The axisymmetric meshes are initially generated as two-dimensional grid with one, equally spaced cell in the third direction like the two-dimensional meshes. Subsequently, the "setup_taugrid"-tool is used to modify the cell width gradually to match a wedge of $1°$. Therefore, the width of the cells grows in radial direction (see fig. 2.12, right). Since the first element at the center cannot be infinitely small, the first cell's depth is set to $1 \cdot 10^{-8}$ m.

2.4 Experimental Results used for Validation

The axisymmetric intake was studied experimentally by Dr. Dirk Herrmann and Mr. Martin Achner simultaneously to this study in the Trisonic Test Section (TMK) facility of the Supersonic and Hypersonic Technologies department of DLR in Cologne. The tests were conducted with a total temperature of $T_{\mathrm{t}} \approx 300$ K and dynamic pressure of $q \approx 10^5$ Pa. This study refers to experiments conducted at $M_\infty = 3.5$ and $M_\infty = 4$ leading to unit Reynolds numbers of $Re_{\mathrm{u}} = 5.16 \cdot 10^7$ m^{-1} and $Re_{\mathrm{u}} = 6.19 \cdot 10^7$ m^{-1}.

During the tests the cone could be traversed, changing x_{c}. Since the cowl is parallel to the free flow at the throat area A_{t}, x_{c} only changes A_{cl} while A_{t} is kept constant. Thus, the contraction ratio CR_{i} is a function of x_{c} as depicted in figure 2.13. The model was equipped with probes for measuring wall pressure and stagnation pressure. In addition, Schlieren images of the external flow were taken with a frequency of 500 Hz.

Within this study, the experiments were used to obtain critical configurations for which the intake starts or unstarts. The experiments that were conducted to analyze starting were initialized from unstarted mode. Subsequently, the cone was traversed upstream, decreasing CR_{i}, until the intake started. Starting was detected by the sudden drop of wall pressures in a post-experiment analysis and the corresponding cone position x_{c} was extracted. In total three experiments for $M_\infty = 4$ and two for $M_\infty = 3.5$ were performed. The experiments showed only small scattering: The maximum deviation was found for $M_\infty = 4$ as $\Delta x_{\mathrm{c}} = 0.14$ mm and for $M_\infty = 3.5$ as $\Delta x_{\mathrm{c}} = 0.03$ mm. The rounded mean values are shown in table 2.3. The value of x_{c} at $M_\infty = 4$ was obtained in prior experiments. Furthermore, Schlieren images and wall pressure values at ramp and cone were obtained for $x_{\mathrm{c}} = 144.6$ mm and $M_\infty = 4$ in started mode.

Mach number	case	x_c [mm] (1. run)	x_c [mm] (2. run)	x_c [mm] (3. run)	Δx_c [mm]
$M_\infty = 4$	starting	144.14 mm	144.0 mm	144.10 mm	0.14 mm
	unstarting	$\approx$ 130 mm	-	-	-
$M_\infty = 3.5$	starting	-	147.73 mm	147.70 mm	0.03 mm

Table 2.3: Cone positions for starting and unstarting according to experiments

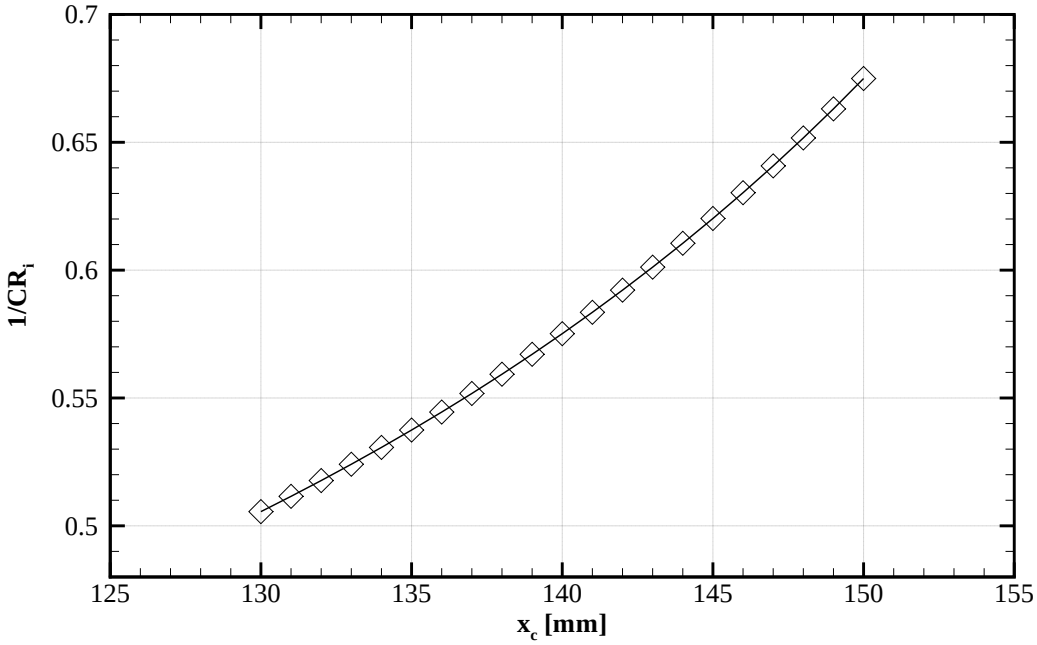

Figure 2.13: Internal contraction ratio plotted against the cone position for the axisymmetric intake

3 Results

3.1 Validation

The obtained numerical results were compared to experimental and analytical data. Special attention was paid to the starting and unstarting behavior. Additionally, wall pressures and shock positions have been analyzed in order to assess whether the general flow behavior is predicted correctly by the CFD simulations.

3.1.1 Comparison with Axisymmetric Experiments

Starting and Unstarting Behavior

In the experiments, starting and unstarting was provoked by traversing of the cone at constant free stream Mach number M_∞ (see ch. 2.4), whereas M_∞ was varied in the numerical approach. In the experiments, starting for $M_\infty = 4$ occurred at $x_\mathrm{c} = 144.1\ \mathrm{mm}$ ($CR_\mathrm{i} = 1.63$). Therefore, this cone position was analyzed in the numerical study in terms of starting. As both approaches are quasi-steady, the numerical simulation should consequently predict starting for $M_\infty = 4$. The cone position $x_\mathrm{c} = 147.7\ \mathrm{mm}$ ($CR_\mathrm{i} = 1.54$), which produced starting at $M_\infty = 3.5$ in the experiments, was analyzed with the same approach. For unstarting, experimental data was only available for $M_\infty = 4$, where unstart occurred at $x_\mathrm{c} \approx 130\ \mathrm{mm}$ ($CR_\mathrm{i} \approx 2$). Therefore, this cone position was analyzed for unstarting by decreasing M_∞. All values of M_cl in the Kantrowitz plot correspond to the started mode for the corresponding cone position. Since M_cl was not measured in the experiments, values from CFD for the same x_c and M_∞ were used instead.

Figure 3.1 shows the experimentally determined starting limits for $M_\infty = 3.5$ and $M_\infty = 4$ as filled squares (or diamond) and the unstarting limit for $M_\infty = 4$ as unfilled square. The equivalent numerical results to the three experimental configurations and the results for the shock-on-lip configuration for $M_\infty = 4$ ($x_\mathrm{c} = 144.6\ \mathrm{mm}$) are displayed as triangles.

It is obvious, that the numerical simulations predict slightly higher M_cl (up to 8% for starting and up to 10% for unstarting) than the experiments. This deviation may be caused by errors in the model, but may also result from experimental imperfections like unsteady flow conditions or the observed oscillation of the centerbody in unstarted flow, that is not modeled. However, trends are correctly covered.

The amount of the deviation between experimentally measured unstart at $M_\infty = 4$ and numerically predicted unstart for the equivalent cone position $x_\mathrm{c} = 130\ \mathrm{mm}$ of $\Delta M_\mathrm{cl,unstart} = 10\%$ may be caused or intensified by the particularly complex flow for this configuration: For $x_\mathrm{c} = 130\ \mathrm{mm}$ and $M_\infty \geq 4$, the cone shock impinges inside of the cowl and consequently interacts with the boundary layer, thus causing local boundary layer detachment. For the configuration with $x_\mathrm{c} = 144.6\ \mathrm{mm}$, however, the predicted unstart levels intersect with a fitted empirical limit of Flock [13], that replicates general trends within the Kantrowitz plot well. Therefore, this might indicate, that predictions of unstart are more precise for configurations, where the cone shock does not impinge inside of the cowl. However, one should keep in mind, that the empirical limit of Flock was developed to predict starting (not unstarting).

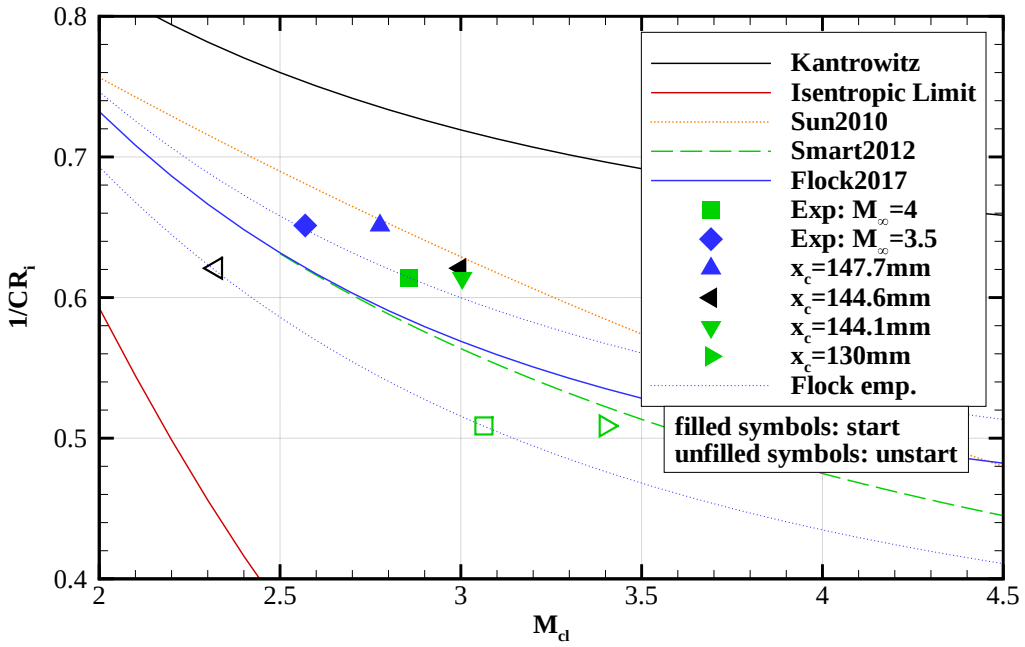

Figure 3.1: Experimental and numerical configurations for starting and unstarting

Wall Pressure

Figure 3.2 shows the averaged and normalized wall pressures measured at the ramp and the numerically calculated normalized pressures. Both are presented for $M_\infty = 4$ and started mode with $x_\mathrm{c} = 144.6$ mm. The averaging was done for $\Delta t = 2$ s during steady conditions. The variations that occur during the averaging span are depicted as error bars. The comparison with the numerical Schlieren at the bottom of figure 3.2, shows that each pressure peak corresponds to the impingement of a shock wave on the wall.

The tendencies of the wall pressure and thus the locations of the internal shocks are predicted well by the CFD simulation. However, at the cone a deviation of $\Delta p/p_\mathrm{st} \approx 10\%$ exists.

Shock Positions

During the experiments Schlieren images were recorded at 500 Hz. Figure 3.3 shows an experimental Schlieren image that was obtained by averaging 50 consecutive images for $x_\mathrm{c} = 144.6$ mm $= const.$ and $M_\infty = 4$. Numerical Schlieren for the same flow conditions are superimposed to the picture of the experimental Schlieren. The experimental Schlieren were recorded as line of sight measurement technique of a three-dimensional flow. Therefore, the experimental density gradient appears slightly broadened compared to the numerical density gradient that is fully two-dimensional. The shock positions of the cone shock and the external cowl shock agree between experiment and CFD.

The internal flow is concealed by the cowl and thus is not visible in the Schlieren images. Hence, only the external part of the flow, which is dominated by inviscid phenomena, can be validated by this method. Therefore, it can be concluded that the CFD is capable of accurately capturing the inviscid dominated flow characteristics of axisymmetric flow in started intakes.

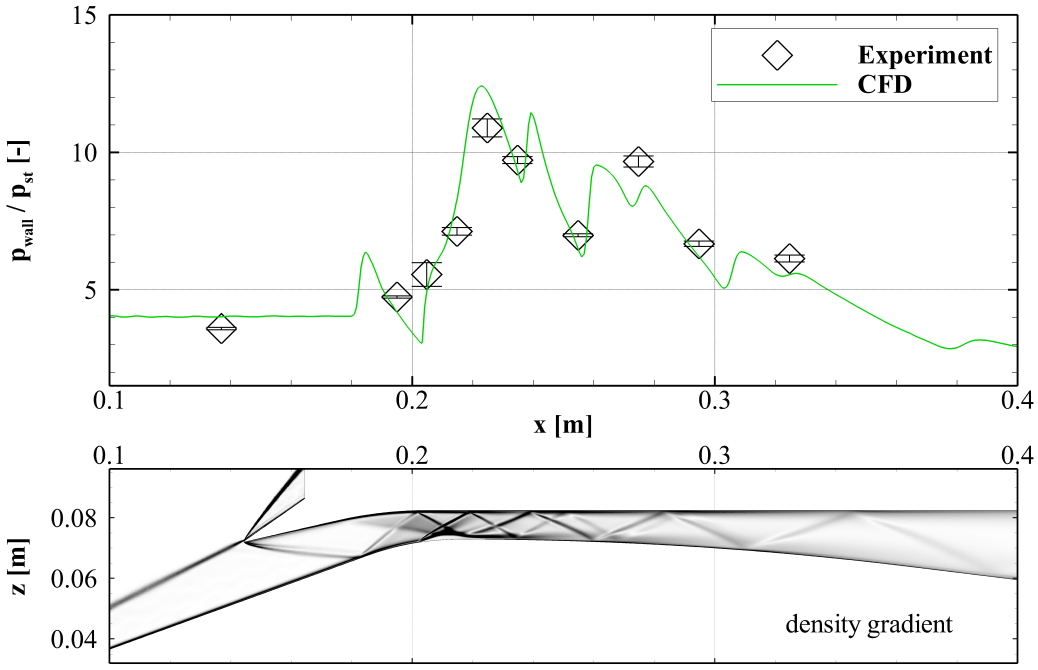

Figure 3.2: Experimentally measured and numerically calculated wall pressure at the center-body of the axisymmetric intake and numerical Schlieren for axisymmetric intake at $M_\infty = 4, x_c = 144.6$ mm

For unstarted flows, an equivalent comparison is not possible, since the position of the detachment is highly unsteady. A comparison to steady simulations is therefore arbitrary and thus not meaningful. However, the CFD correctly predicts the unstarted flow to contain a separation bubble and an oblique shock (compare ch: 1.2.4).

3.1.2 Comparison with Analytical Solutions

Analytical solutions have been derived with the assumption of inviscid flows for the 2D intakes by using the analytical shock relations derived in section 1.2.2. In order to prove that the flow solver accurately captures inviscid flows, Euler simulations have been performed for the design point of the intake. As seen in figure 3.4, the wall pressure is predicted accurately according to the analytical solution.

The most significant deviation is located at the end of the ramp, where the cowl-shock impinges on the wall. Whereas the analytical solution assumes an infinitely small shock, the shock predicted by the CFD has a finite thickness and is therefore partially reflected at the corner. Additionally, the corner produces a small expansion area resulting in a locally small drop in wall pressure.

In conclusion, it was shown, that the CFD is able to accurately predict the inviscid behavior of the flow in areas where the assumptions for the analytical solution are valid.

3.2 Mesh-Independence Study

A mesh-independence study was performed for the meshes with prism layers for one cone position of the axisymmetric intake. These studies were performed on representative test geometries. For the two-dimensional case, the intake with $M_{\infty,\mathrm{DP}} = 8$, $\Pi_{\mathrm{st,DP}} = 10$ and $n_{\mathrm{ramps}} = 3$ was chosen. The

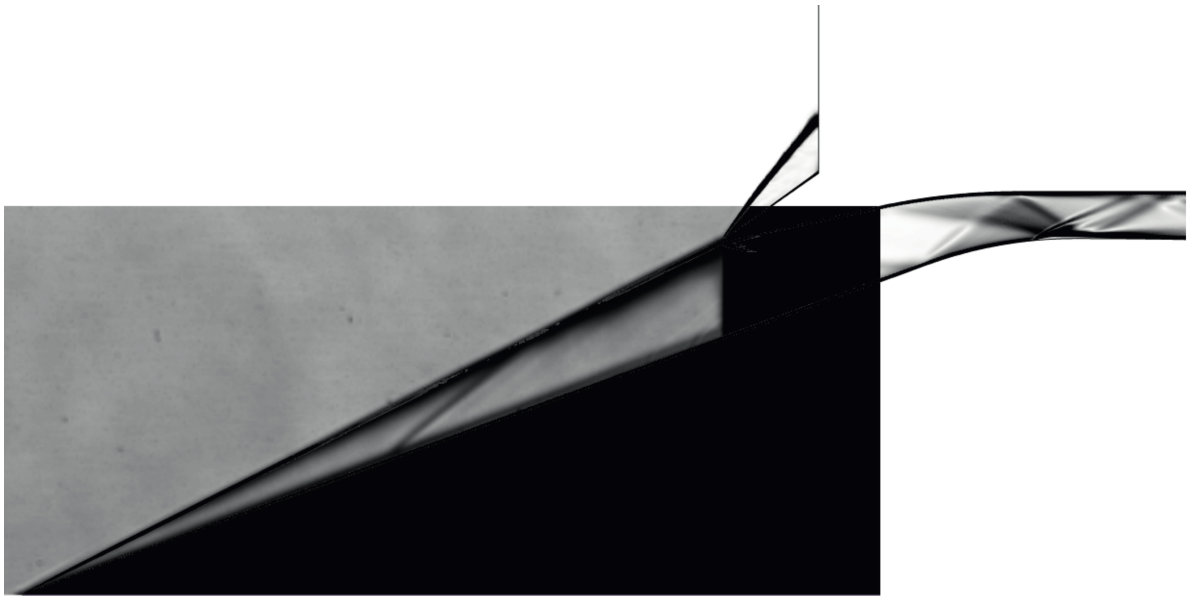

Figure 3.3: Superposition of numerical Schlieren and experimental Schlieren of axisymmetric intake for $x_c = 144.6$ mm and $M_\infty = 4$

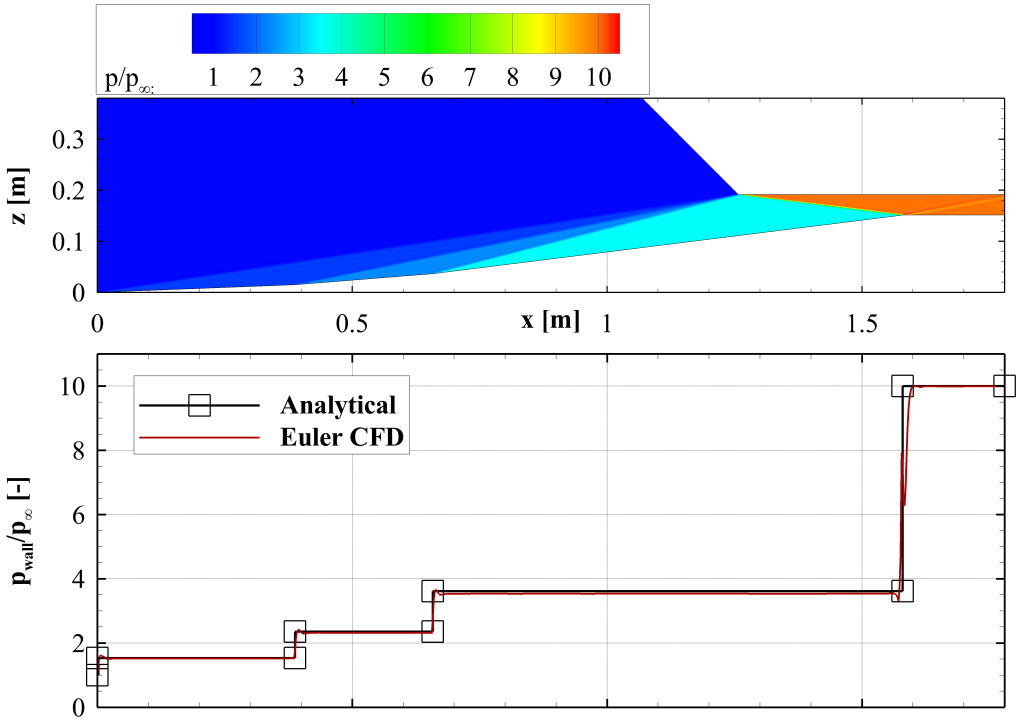

Figure 3.4: Normalized wall pressures in inviscid 2D-Flow obtained from analytical and numerical Euler solution. Generic 2D-intake with $M_{\infty,\mathrm{DP}} = 8$, $\Pi_{\mathrm{s,DP}} = 10$ and $n_{\mathrm{ramps}} = 3$

axisymmetric intake was analyzed for the cone position $x_c = 144.6$ mm. The refined and coarsened meshes have been derived from the reference mesh. Table 3.1 lists the analyzed meshes and their size. The presented relative mesh size is the ratio of the number of elements of the current mesh compared to the reference mesh. A detailed overview of the input parameters of the reference mesh can be found in the Appendix.

Figure 3.5 shows the predicted values of M_{cl} for starting (filled) and unstarting (unfilled) plotted into the Kantrowitz plot. Whereas the coarse meshes predict lower M_{cl} than the reference mesh, the reference and the refined meshes all predict starting and unstarting for the same M_∞. Thus, values of M_{cl} agree within 0.01%. However, keep in mind, that M_∞ was increased in 0.1-increments and therefore the numerical uncertainty for detecting the correct M_{cl} is 0.1.

The distribution of wall pressure predicted by the analyzed meshes are shown in figure 3.6 for the centerbody and the internal part of the cowl. The analyzed case is again $x_c = 144.6$ mm at M_∞ in started mode. In general, all meshes except the most coarsened "coarse3" agree well on the wall pressure distribution both on cowl and centerbody. "coarse3" under predicts the intensity of the reflected shocks, which leads to bigger discrepancy in downstream areas. Whereas the less coarsened "coarse2" still shows minor deviations, the reference and the refined meshes agree well on the pressure distribution. The biggest deviation between the reference and the finest mesh "fine2" occurs at the peak at $x \approx 0.28$m on the centerbody with a discrepancy of 1.8%. This maximum deviation was found to be acceptable.

Figure 3.7 shows the mass capture ratio MCR and the static pressure ratio Π_s measured at the intake throat for the meshes "coarse2", "reference" and "fine2". This type of plot will be discussed in detail in chapter 3.3.2. At this point, it is sufficient to illustrate that the reference and the finest mesh show good agreement on the capturing characteristics, which are among others sensitive to the location of flow separation, and the static pressure ratio both in started and unstarted mode. The most coarse mesh, however, shows more significant deviations from the other meshes in addition to the lowered cowl Mach numbers for starting and unstarting. These are especially distinct around $M_\infty = 4$. Furthermore, the solution of the coarse mesh shows an anomaly at $M_\infty = 4$ of where the mass capture ratio slightly exceeds 1 – both for accelerating and decelerating flow.

In conclusion, the reference mesh showed no deviation in the prediction of starting and unstarting within the accuracy of the applied step size and only little deviation in measured wall pressure to the refined meshes. Therefore, it was concluded, that the solution is sufficiently independent of mesh size. The reference parameters were applied to other configurations without performing additional mesh independence studies, since the flow parameters were assumed to be sufficiently similar.

Mesh	coarse3	coarse2	coarse1	reference	fine1	fine2
			Axisymmetric			
Total Elements	105772	172439	188668	343456	352105	479467
Relative Mesh Size	30.8%	50.2%	54.9%	100%	102%	139.6%
			Two-Dimensional			
Total Elements	-	23719	60272	166627	176270	304106
Relative Mesh Size	-	14.2%	36.2%	100%	105.8%	182.5%

Table 3.1: Meshes analyzed for mesh independence study with absolute element numbers and relative to the selected reference mesh

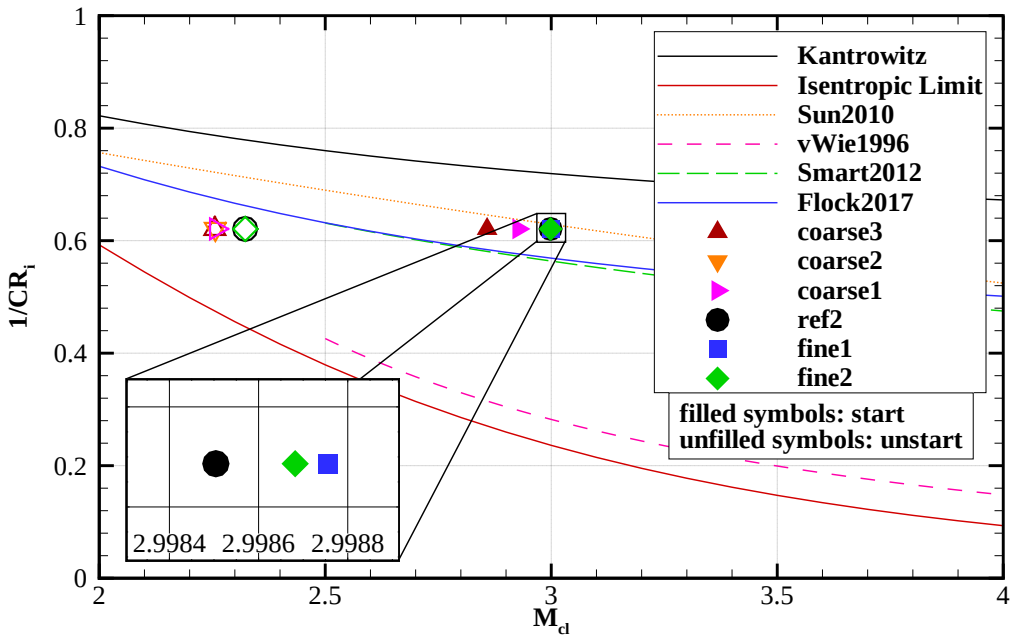

Figure 3.5: Influence of mesh size on starting and unstarting in Kantrowitz plot for axisymmetric intake with $x_c = 144.6$ mm

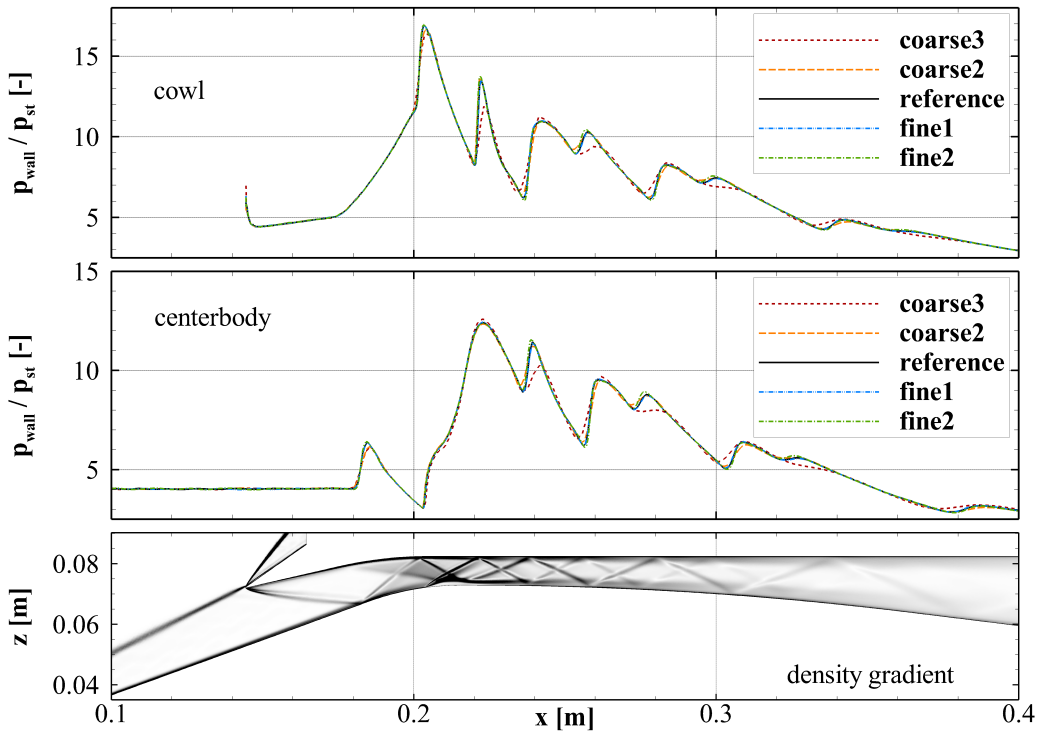

Figure 3.6: Influence of mesh size on wall pressure at cowl (top) and centerbody (middle) of axisymmetric intake. Numerical Schlieren of reference mesh (bottom). All for $x_c = 144.6$ mm, $M_\infty = 4$

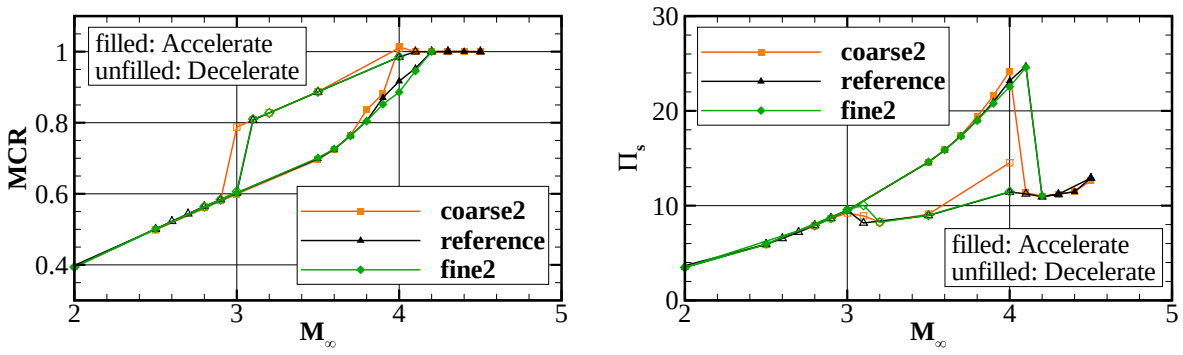

(a) Mass Capture Ratio

(b) Static pressure ratio

Figure 3.7: Influence of mesh size on one-dimensional parameters at A_{th} for axisymmetric intake at $x_{\mathrm{c}} = 144.6$ mm

3.3 Phenomenology

3.3.1 Starting and Unstarting with Free Stream Mach Number

The axisymmetric intake is started and unstarted by variation of free stream Mach number M_∞. Figure 3.8 shows the flow field for selected M_∞ during deceleration for a fixed cone position of $x_{\mathrm{c}} = 144.6$ mm. The first flow field (fig. 3.8(a)) belongs to the case of $M_\infty = 4$ in started mode, which was used for validation of wall pressures and shock positions (compare ch. 3.1.1). For this case, the cone shock impinges at the cowl tip, which is called "shock-on-lip" configuration. The cowl shock, that redirects the flow according to the relative internal cowl angle impinges at the cone and is alternatingly reflected by cone and cowl. At $x \approx 0.21$ m, the boundary layer at the center body separates due to the impingement of the reflected cowl shock and reattaches at $x \approx 0.22$ m. The small separation induces two additional shocks, that emanate from the separation and the reattachment location. These two shocks are also reflected by both walls.

The second case in figure 3.8(b) is decelerated to $M_\infty = 3.1$ and is close to unstarting. Due to the reduced Mach number, the angles of cone and cowl shock are increased. Consequently, the impingement of the twice reflected cowl shock moves upstream, which causes the separation bubble to move upstream. Furthermore, the strength of the shocks is decreased, which can be seen by the reduced intensity in the numerical Schlieren images.

If the Mach number is further decreased to $M_\infty = 3$ (fig. 3.8(c)), the flow unstarts. The flow spillage is accomplished by an oblique shock wave, that emanates from a separation bubble that spans from $x \approx 0.12$ m to $x \approx 0.19$ m. Note that this unstart mode cannot be captured in inviscid simulations. The separation is accompanied by a strong shock that interacts with the separation bubble at $x \approx 0.15$ m and induces a subsonic region downstream of the shock. Furthermore, it raises the pressure above the level within the separation bubble. Therefore, the separation bubble is narrowed in the subsequent downstream region and the remaining flow is accelerated to partially supersonic speeds. The reduced pressure in the supersonic parts of the internal flow again causes the formation of shocks at $x \approx 0.17$ m accompanied by a small separation bubble. At the throat the flow is supersonic in the central region and subsonic in the proximity of the walls. In the following diffusor, the flow is accelerated to supersonic speeds due to low back pressure in the simulations.

If the flow is further decelerated, the detachment shock angle increases (see fig. 3.8(d)) and eventually becomes a strong shock. In addition, the strong shock on top of the separation bubble vanishes. Finally the separation bubble disappears and thus the unstart mode changes to strong shock without flow separation (fig. 3.8(e)). The flow downstream of the strong shock stays subsonic until the throat.

If the flow is accelerated from unstarted mode, it restarts at a M_∞ that is larger than the free stream Mach number where unstart occurred. This creates a hysteresis. This acceleration is depicted in figure 3.9. Before the intake restarts, the location of the angle of the oblique shock decreases due to increased Mach number. This can be seen for $M_\infty = 4.1$ in fig. 3.9(a). Furthermore, the location of separation and therefore the location of the oblique shock move downstream. Both effects reduce the spillage mass flow. The increased M_∞ also causes the internal shocks to become more intense, which enlarges the separation bubble at the cowl both in length and height.

If the Mach number is increased to $M_\infty = 4.2$, the intake restarts leading to a similar flow field as for the shock-on-lip case (fig. 3.8(a)). Due to the slightly higher M_∞, the cone shock impinges inside the cowl, and is reflected like the cowl shock.

Further acceleration causes the cone shock to impinge further downstream. For $M_\infty = 4.5$ (fig. 3.9(c), the reflected cone shock impinges at the separation bubble at $x \approx 0.2\ \mathrm{m}$ and thereby increases the separation length.

Higher free stream Mach numbers have not been studied, since no further change of flow mode is expected. Furthermore, flow conditions with an internally impinging cone shock are avoided during operation. Therefore, further increased Mach numbers in connection with the studied intake and especially at this cone position have low relevance for practical use.

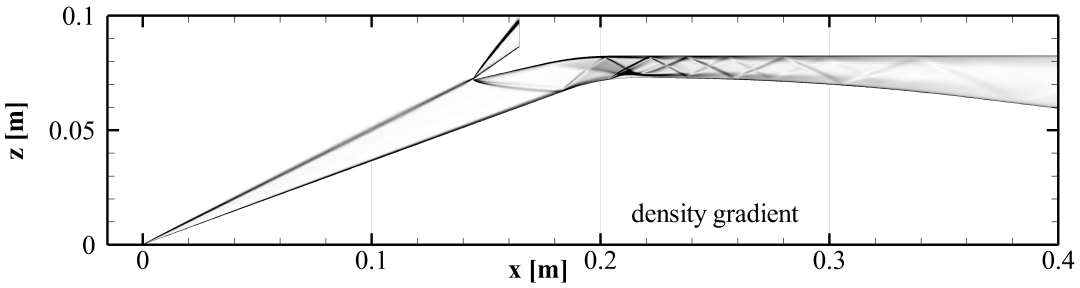

(a) $M_\infty = 4$ started

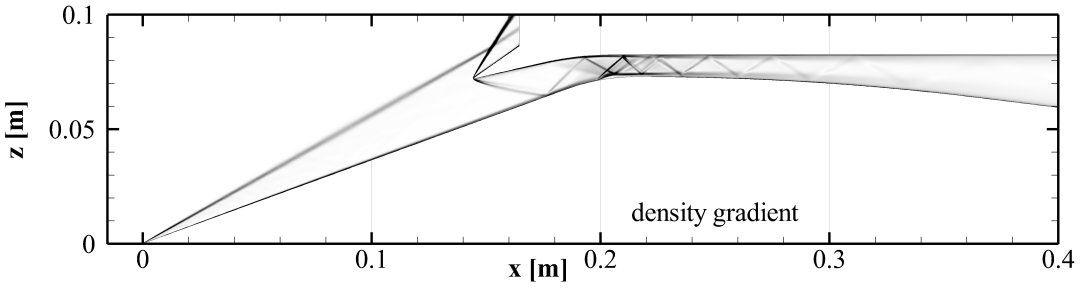

(b) $M_\infty = 3.1$ started - right before unstarting

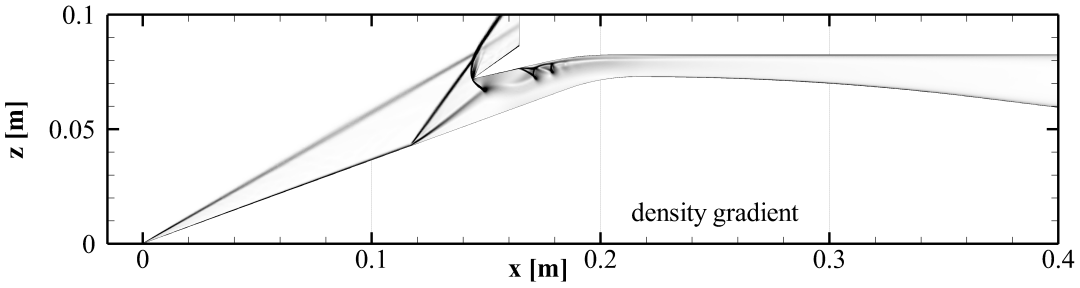

(c) $M_\infty = 3$ unstarted - right after unstarting

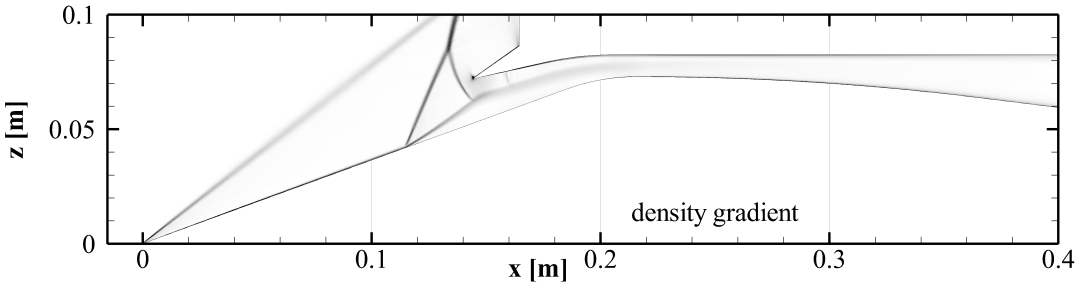

(d) $M_\infty = 2$ unstarted

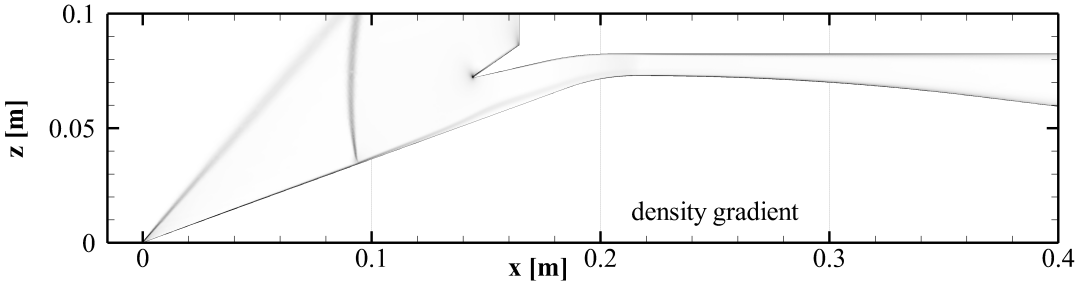

(e) $M_\infty = 1.5$ strong shock unstart

Figure 3.8: Numerical Schlieren of unstarting process for $x_c = 144.6$ mm

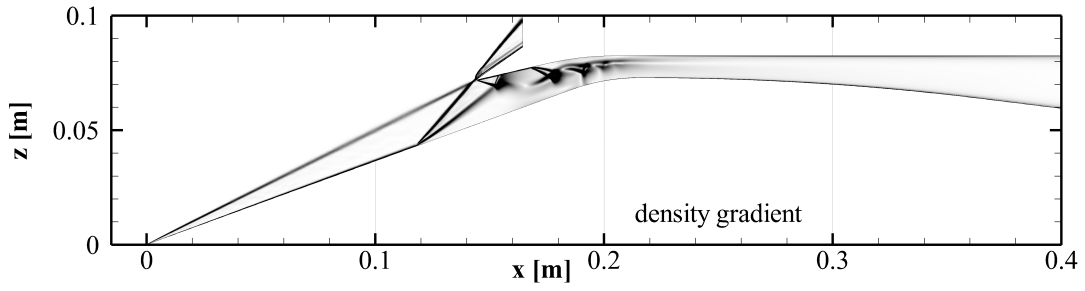

(a) $M_\infty = 4.1$ unstarted - right before starting

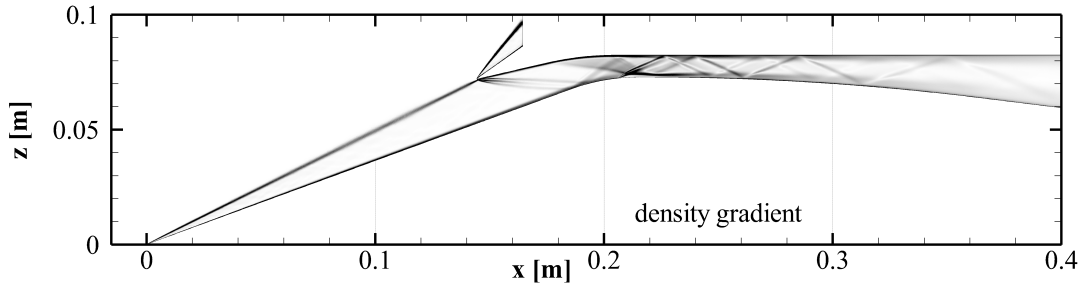

(b) $M_\infty = 4.2$ started - right after starting

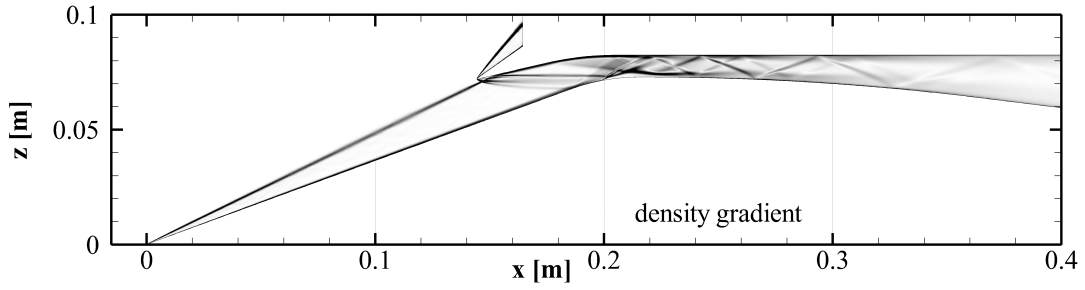

(c) $M_\infty = 4.5$ started

Figure 3.9: Numerical Schlieren of starting process for $x_c = 144.6$ mm

3.3.2 Effect of Viscosity

As stated before, inviscid simulations are not able to capture unstarted flow with flow separation and an oblique shock. The two-dimensional ramp intake with $M_{\infty,\mathrm{DP}} = 8$, $\Pi_{\mathrm{st,DP}} = 10$ and $n_{\mathrm{ramps}} = 3$ has been analyzed both with an inviscid Euler simulation and a viscous RANS simulation. As depicted in the *Kantrowitz plot* in fig. 3.10, the Euler simulation predicts the critical M_{cl} for starting nearly twice as high as the RANS simulations. The strong shock that is predicted with Euler simulations resembles the assumption of a normal shock as in the Kantrowitz criterion and is therefore conservative. The oblique shock that forms due to viscosity, however, is more similar to the assumption of a nearly detached oblique shock in Flock's criterion. Consequently, starting is predicted in the proximity of Flock's criterion by the RANS equations. According to the Kantrowitz criterion, an intake with this internal contraction ratio ($CR_{\mathrm{i}} \approx 2$) should not be self-starting for any Mach number. However, also the Euler simulation predicts that, at least for high Mach numbers, the intake will start. This may be due to the interaction of the ramp shocks and the strong shock. Starting is predicted for $M_{\infty} = 8.4$, which is bigger than $M_{\infty,\mathrm{DP}}$, so the ramp shocks interact with the strong shock upstream of the internal inflow.

In contrast to starting, unstarting is predicted similarly for Euler and RANS solutions. This means that even though the unstarted flow is dominated by viscosity, the unstart mechanism is nearly independent of viscosity. The slightly higher M_{cl} in the RANS solution may be due to less uniformity caused by viscous losses in the boundary layer.

Figure 3.11 shows one-dimensional parameters at the outflow plane of the numerical domain, that were extracted with *AEX1D* (see ch. 2.1.4). Every symbol (here triangles and diamonds) corresponds to a converged solution of an individual steady state simulation. Filled symbols represent decelerating in terms of M_{∞} and unfilled symbols correspond to an acceleration. The mass capture ratio (fig. 3.11(a)) is useful to illustrate the characteristics of the hysteresis between started and unstarted mode, since in general, the mass capture ratio during started mode is bigger than for unstarted mode. In the case of acceleration from unstarted mode, the intake starts at $M_{\infty} = 4.5$ for the viscous and $M_{\infty} = 8.4$ for the inviscid case, which results in a significant step towards higher mass capture ratios. Unstarting on the other hand, can be identified by the step in terms of mass capture ratio at lower M_{∞}. As long as $MCR < 1$, the mass capture ratio is increased approximately linearly with increased M_{∞} both for stared and unstarted mode. $MCR = 1$ is reached for the shock-on-lip case. Any further increase of M_{∞} does not affect MCR and the ramp shock(s) impinge at the internal section of the cowl. For the viscous case, the hysteresis is not closed for started flow, since the deceleration was initialized for $M_{\infty} = 3$, which is slightly above $M_{\infty,\mathrm{unstart}} = 2.7$. This is done in order to reduce unnecessary steps in non-critical regions and has no effect on the prediction of starting or unstarting as described in chapter 2.1.1. In general, the mass capture ratio is reduced for viscous flow compared to inviscid simulations. For started mode, this is caused by increased shock angles due to interaction with the boundary layer. For unstarted mode the difference is increased by the significant blockage due to the separation bubble. This means, that the spillage mass flow is bigger for the viscous case. The difference between viscid and inviscid MCR further increases with increasing M_{∞}, which corresponds to increasing boundary layer thickness.

Figure 3.11(b) shows the static pressure ratio Π_{s} between the ambient state and the exit plane of the isolator A_{out}. Π_{s} generally increases with increasing M_{∞} and is bigger for started than for unstarted mode, since the flow is further decelerated in unstarted mode. The step for unstarting is significantly larger as for starting, since Π_{s} increases faster with M_{∞} during unstarted mode. This figure demonstrates that this intake would not be a feasible option, if inviscid flow applied, since static pressure ratios of more than ten times the design pressure ratio are exerted on the intake before starting. For viscous flow, the maximum static pressure ratio is $\Pi_{\mathrm{s}} \approx 15$ and thus only 150% of the design pressure ratio. This is due to the lower $M_{\infty,\mathrm{starting}}$ and the generally lower static pressure ratios of unstart with an oblique shock in

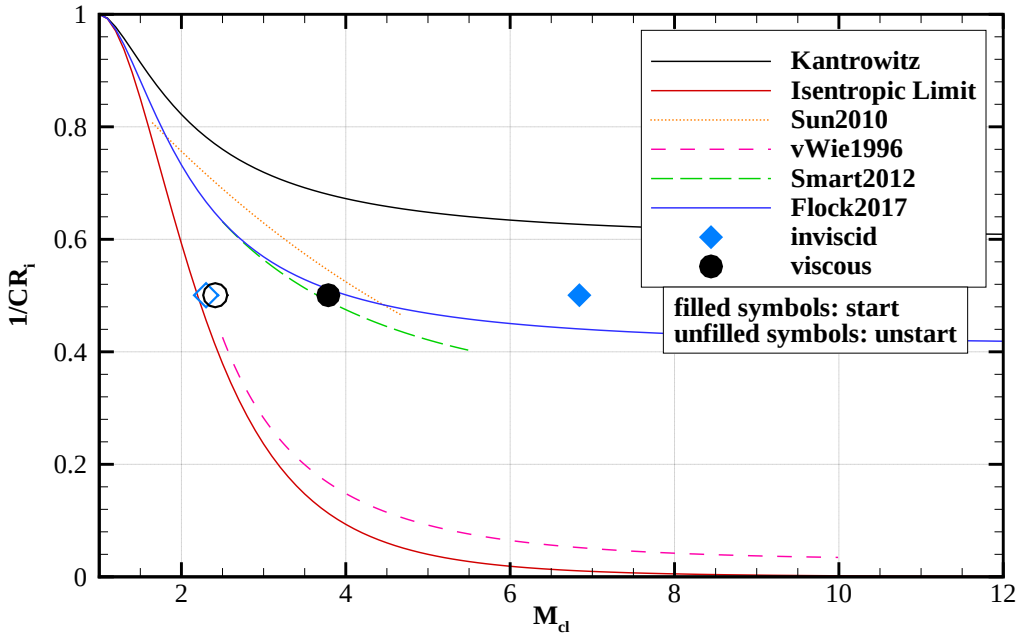

Figure 3.10: Effect of viscosity in Kantrowitz plot for two-dimensional ramp intake with $M_{\infty,\mathrm{DP}} = 8, \Pi_{\mathrm{DP}} = 10, n_{\mathrm{ramps}} = 3$

contrast to unstart with a strong shock.

The total pressure recovery Π_t, that is plotted in figure 3.11(c) also shows a distinct hysteresis. For unstarted mode, Π_t is, due to increased shock losses and potentially viscous losses, significantly lower than for started mode. Π_t is generally lower for the viscous case due to viscous losses. For unstarted flow, this deviation is reduced due to the large shock losses across the normal shock for inviscid unstart. The lowered total pressure recovery for viscous flows has to be considered, if a preliminary intake design is done using Euler simulations. Furthermore, this figure emphasizes the significance to operate an intake in started mode, even though the difference between started and unstarted mode in terms is less intense for viscous flow.

The static temperature ratio Θ_s, which is depicted in figure 3.11(d), generally exhibits a similar trend as Π_s. Consequently, the intake is subject to high thermal loads at high Mach numbers during unstarted mode, additional to the mechanical loads. These thermal loads are not critical for wind tunnel tests in cold gas facilities, since the total temperature cannot be exceeded. For flight conditions, however, the thermal loads can become critical for efficiency and eventually material constraints.

A remarkable difference between the unstart modes can be seen in fig. 3.11(e): Whereas the flow at A_cl is fully subsonic with constant M_cl for an unstart with a strong shock, M_cl is increasing with M_∞ for the unstarted mode with an oblique shock. As a consequence, the flow is predominantly supersonic at A_cl prior to starting in the viscous case. For started mode, M_cl is only slightly reduced due to viscous effects.

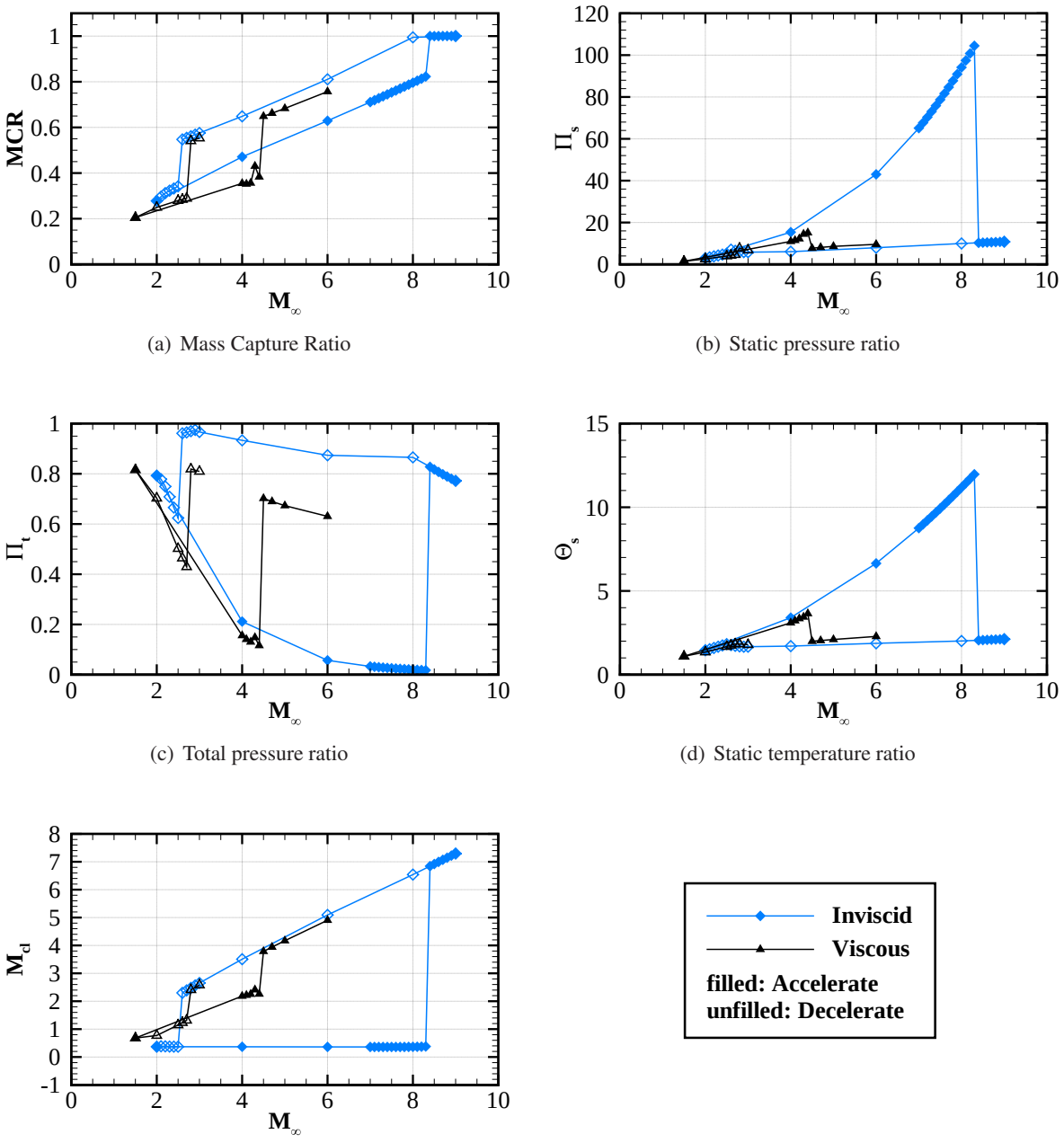

(a) Mass Capture Ratio

(b) Static pressure ratio

(c) Total pressure ratio

(d) Static temperature ratio

(e) Cowl Mach number

Figure 3.11: Starting and Unstarting with Flow Angle for two-dimensional intake with $M_{\infty,\mathrm{DP}} = 8, \Pi_{\mathrm{DP}} = 10, n_{\mathrm{ramps}} = 3$ at $M_\infty = 8$ at A_{out}

3.3.3 Starting and Unstarting with Pitch Angle

Starting and unstarting can also be caused by pitch angle. This phenomenon is studied for a two-dimensional intake ($M_{\infty,\mathrm{DP}} = 8$, $\Pi_{\mathrm{st,DP}} = 10$, $n_{\mathrm{ramps}} = 3$) at $M_\infty = 8$ with an Euler simulation. The results are presented in figure 3.12 for the entry plane of the internal flow A_{cl} and the end of the isolator A_{out}.

For negative pitch angles, the relative angle between ramps and free stream increases and thus the compression increases and Mach numbers downstream of the shocks decrease (see figures 3.12(b), 3.12(e)). Hence, the intake unstarts for a pitch angle of $\alpha = -30°$. If pitch angles are increased, the relative ramp angles decrease and eventually become negative, so the flow is not compressed but expanded at the first ramp. The resulting acceleration causes the intake to restart at $\alpha = -3°$. Note, that the first ramp's angle only measures $\delta = 2°$. Consequently, the stagnation point would be at the bottom side of the ramp (or the other side of the vehicle), which is not part of the numerical domain.

In figure 3.12(a) Mass Capture Ratios of $MCR > 1$ are depicted. This is due to the applied definition of the capture area: A_0 is defined for $\alpha = 0°$ and is not adjusted to pitch angles. As a consequence, the internal mass flow increases for moderately decreased pitch angles and vice versa. The same trend for moderately decreased pitch angles applies to Π_{s} and Θ_{s}. The total pressure recovery Π_{t}, however, has a global maximum for $0°$ and started flow, which is consistent with this being the design configuration of the intake. Mass flow and consequently MCR are equal for both cross sections, since no flow is extracted or added in the internal flow.

The presented variation of pitch angle would expose the intake (and the whole vehicle) to significant aerothermal stresses: The static pressure ratios would exceed 300 at A_{cl} for an intake that is designed for $\Pi_{\mathrm{s}} = 10$ (3.12(b)) and static temperature ratios of above 13 would lead to average temperatures of $T_{\mathrm{s}} > 2800\ K$ even within the tropopause. Therefore, this trajectory is not realistic for operation, but demonstrates the influence of pitch angles. Also keep in mind that these results are obtained from inviscid simulations. For large pitch angles, viscous phenomena should be expected like boundary layer separation.

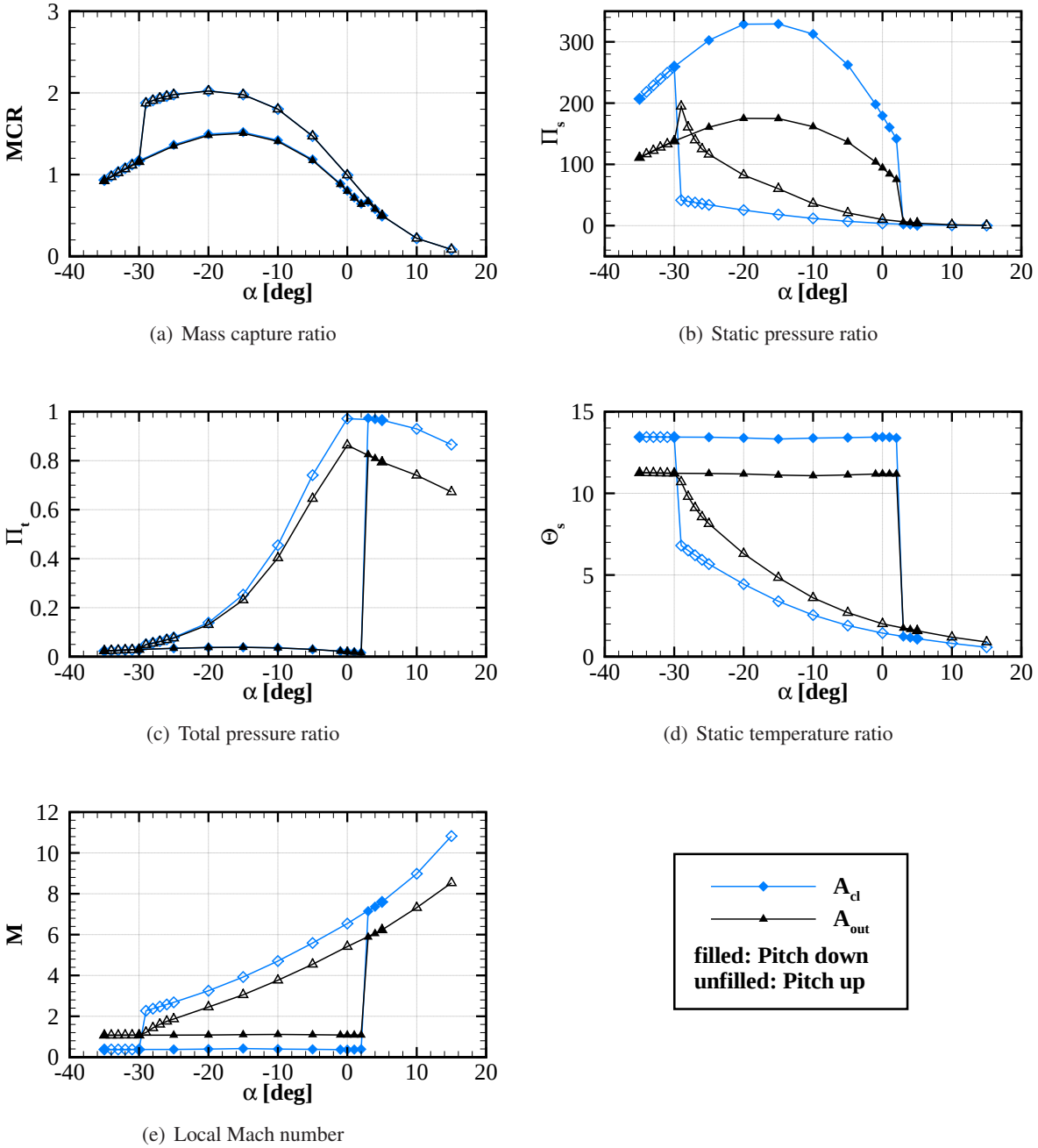

(a) Mass capture ratio

(b) Static pressure ratio

(c) Total pressure ratio

(d) Static temperature ratio

(e) Local Mach number

Figure 3.12: Starting and unstarting with pitch angle for two-dimensional intake with $M_{\infty,\mathrm{DP}} = 8, \Pi_{\mathrm{DP}} = 10, n_{\mathrm{ramps}} = 3$ at $M_\infty = 8$ at A_{cl} and A_{out}

3.4 Parameter Study

A parameter study has been conducted in order to analyze the influence of Reynolds number and relative wall temperature. For this study, the axisymmetric intake is used. The reference conditions are given by the wind tunnel conditions of the experiments in TMK wind tunnel facility (see ch. 2.4). The conditions deviating from the reference were also calculated with the wind tunnel mode (see ch. 2.3.3). However, this does not mean that these conditions can be achieved in the TMK facility.

3.4.1 Reynolds Number

The influence of the Reynolds number Re is studied by varying the dynamic pressure q_∞. As explained in chapter 2.3.3, q_∞ and Re are proportional to each other in wind tunnel mode and thus doubling q_∞ leads to a doubling of Re. However, Re varies slightly with M_∞. Table 3.2 shows the unit Reynolds numbers for the analyzed cases at $M_\infty = 3$ and $M_\infty = 4$, that approximately correspond to unstarting respectively starting.

Figure 3.13 shows starting and unstarting in the *Kantrowitz plot* for varied Re. The figure shows, that unstart is delayed to lower M_{cl} for higher Reynolds numbers and vice versa. For starting, critical M_{cl} is significantly decreased, if Re is increased. This corresponds to the trend for unstarting, although the effect is greater for starting. A decreased Reynolds number, however, does not affect M_{cl} for starting. This result is even more striking, considering the strong influence of the decreased Reynolds number.

Besides its influence on starting, Reynolds number has little effect on the one-dimensional parameters at the throat – especially for started mode (see fig. 3.14). For unstarted mode, the deviations are bigger, but still below 2%. The general tendencies of increased Reynolds number for unstarted mode are to slightly increase Mass capture ratio and pressure recovery and slightly reduce static pressure and temperature ratio.

	$q = 0.5$ bar	$q = 1$ bar	$q = 2$ bar
$Re_{\mathrm{u}}(M_\infty = 3)[\mathrm{m}^{-1}]$	$2.18 \cdot 10^7$	$4.35 \cdot 10^7$	$8.7 \cdot 10^7$
$Re_{\mathrm{u}}(M_\infty = 4)[\mathrm{m}^{-1}]$	$3.09 \cdot 10^7$	$6.19 \cdot 10^7$	$1.24 \cdot 10^8$

Table 3.2: Unit Reynolds numbers for wind tunnel mode for varied dynamic pressure

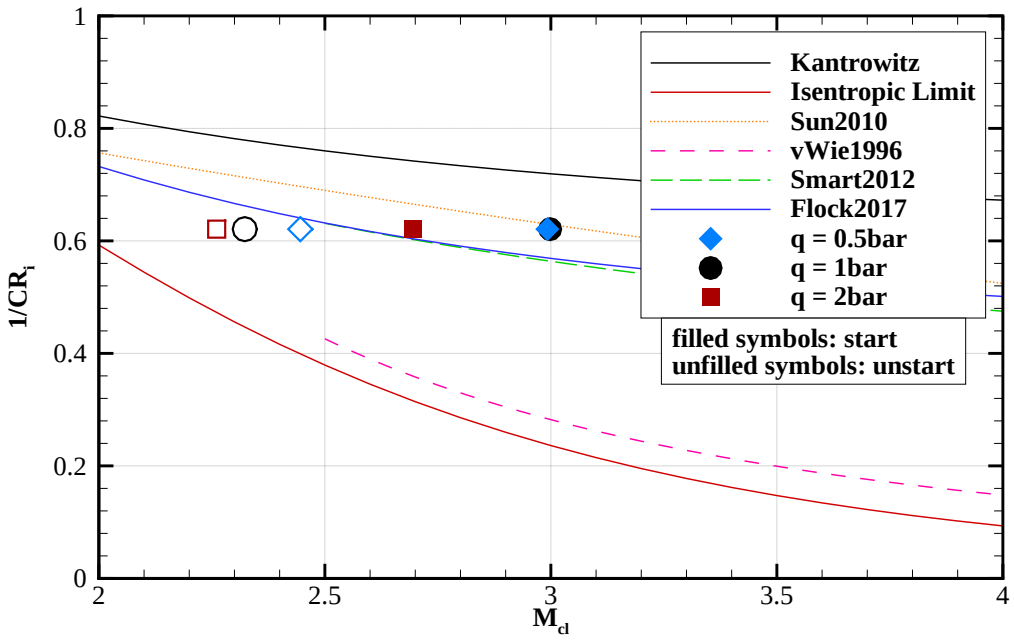

Figure 3.13: Influence of the Reynolds number on starting and unstarting in Kantrowitz plot

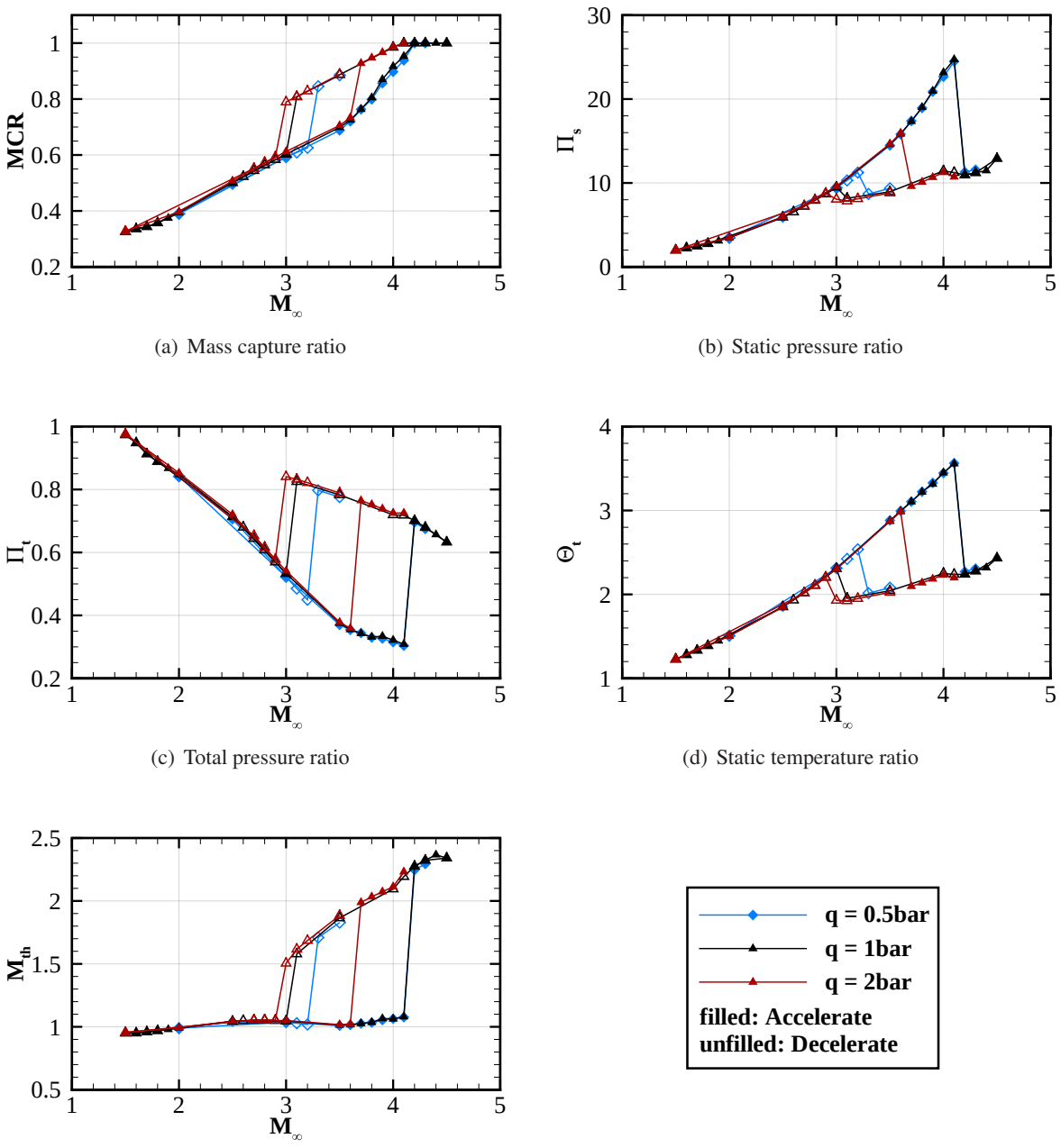

(a) Mass capture ratio

(b) Static pressure ratio

(c) Total pressure ratio

(d) Static temperature ratio

(e) Local Mach number

Figure 3.14: Influence of Reynolds number on one-dimensional parameters for axisymmetric intake at A_{th}

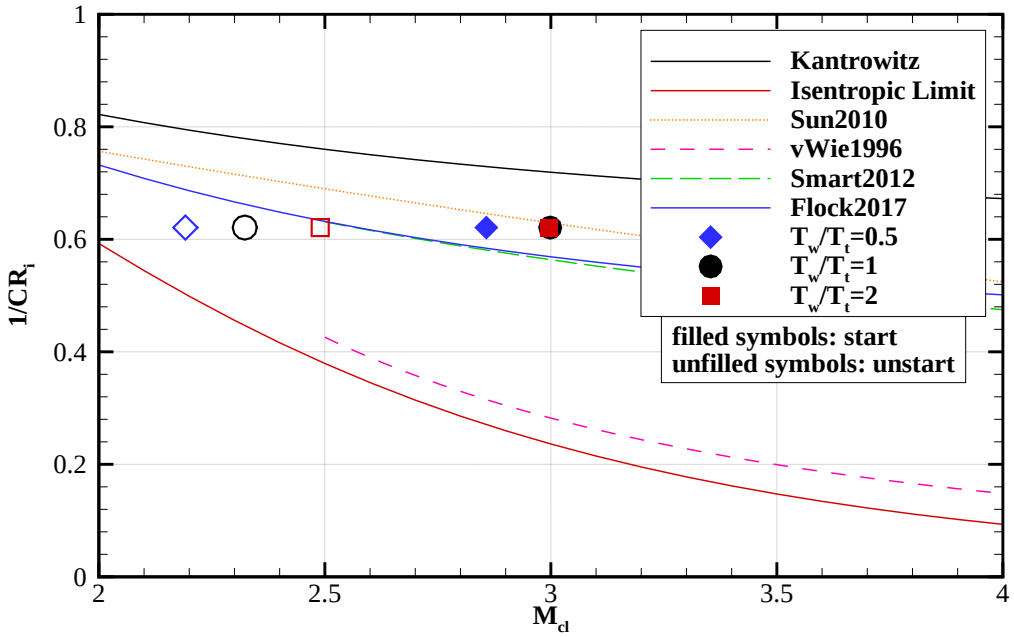

Figure 3.15: Influence of the ratio of wall and total temperature on starting and unstarting in Kantrowitz plot

3.4.2 Relative Wall Temperature

The second analyzed parameter is the relative wall temperature $T_\mathrm{w}/T_\mathrm{t}$. In order to achieve this variation, T_t was varied while T_w was held constant at $T_\mathrm{w} = 300\ K$. For this study, $T_\mathrm{t} = 600\ K$, $T_\mathrm{t} = 300\ K$ and $T_\mathrm{t} = 150\ K$ have been analyzed, which is equivalent to $T_\mathrm{w}/T_\mathrm{t} = 0.5$, $T_\mathrm{w}/T_\mathrm{t} = 1$, $T_\mathrm{w}/T_\mathrm{t} = 2$.

Figure 3.15 shows, the effect of $T_\mathrm{w}/T_\mathrm{t}$ on starting and unstarting. A cooled wall ($T_\mathrm{w}/T_\mathrm{t} < 1$) reduces M_∞ for both starting and unstarting, whereas unstart happens at higher M_∞ for the heated wall. This can be explained by the influence of $T_\mathrm{w}/T_\mathrm{t}$ on the boundary layer. A cooled wall leads to a thinned boundary layer [3, p.244]. A thin boundary layer is less prone to detachment, which again delays unstarting.

Especially within unstarted mode, the relative wall temperature has a strong influence on the one-dimensional parameters as depicted in figure 3.16 For $T_\mathrm{w}/T_\mathrm{t} = 2$, the mass capture ratio is reduced by up to 7%, and the total pressure recovery is decreased up to 6%. It is plausible that in case of a heated wall, the static temperature ratio increases both in started and unstarted mode. The effect of relative wall temperature on the static pressure is twofold: For unstarted mode, a heated wall reduces Π_s, whereas for started mode, Π_s is increased. Both effects of higher relative wall temperature on static pressure ratio are favorable for operation. However, the wall temperature is limited by material constraints.

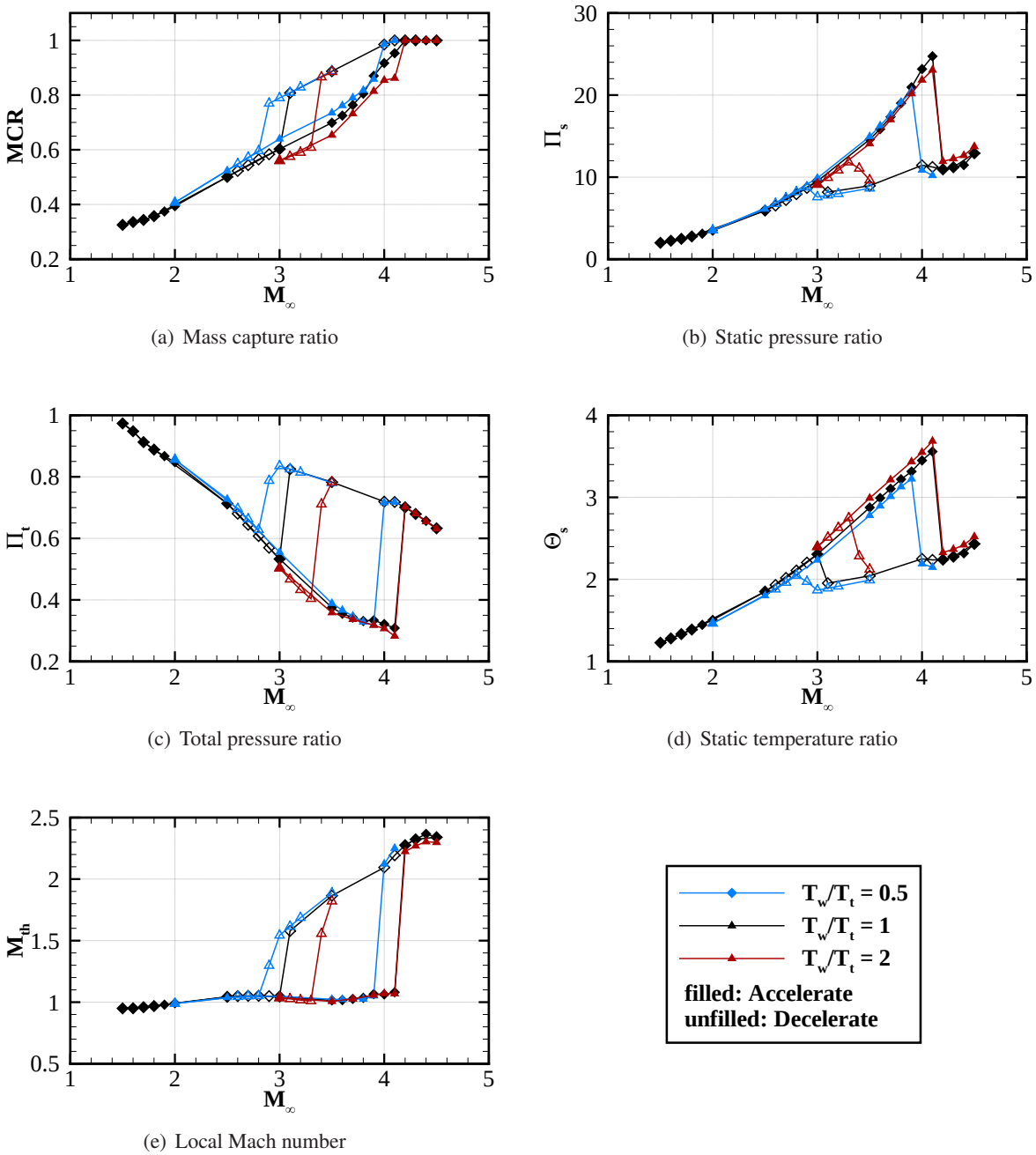

(a) Mass capture ratio

(b) Static pressure ratio

(c) Total pressure ratio

(d) Static temperature ratio

(e) Local Mach number

Figure 3.16: Influence of the ratio of wall and total temperature on one-dimensional parameters for axisymmetric intake at A_{th}

3.4.3 Wind Tunnel Compared to in-Flight Conditions

Finally, the axisymmetric intake was simulated for a flight at $q_\infty = 5.24 \cdot 10^4\ \mathrm{Pa} = \mathrm{const.}$ within earth's atmosphere (see ch. 2.3.3). The relative wall temperature was set to $T_\mathrm{w}/T_\mathrm{t} = 0.5$. Since experiments cannot meet all similarity parameters of super and hypersonic flows and flight experiments are expensive, it is important to know the effects of these deviations in order to ensure correct interpretation of the results. In general, the unit Reynolds numbers during flight at $q_\infty = 0.524\ \mathrm{bar}$ are lower than for wind tunnel conditions. Whereas the Reynolds number decreases during acceleration at supersonic flight and constant dynamic pressure, the Reynolds number increases for $M_\infty > 1.5$ in the cold gas wind tunnel. Consequently, the deviation becomes bigger with increasing Mach numbers. Furthermore, total temperatures are significantly higher for flight conditions compared to the cold gas wind tunnel.

The predicted free stream Mach numbers for starting and unstarting are both lower for flight mode than for wind tunnel conditions with $T_\mathrm{w}/T_\mathrm{t} = 1$ ($\Delta M_\mathrm{cl,start} = 3\%$ and $\Delta M_\mathrm{cl,unstart} \approx 5\%$), which can be seen in figure 3.18. Consequently, real experimental wind tunnel tests without heated flow will likely predict slightly higher Mach numbers for starting and unstarting, than those occurring during real flight. This is a favorable outcome, since lower Mach numbers for starting and unstarting are advantageous for operation, thus making predictions in the wind tunnel conservative. Wind tunnel mode with $T_\mathrm{w}/T_\mathrm{t} = 1$ also predicts lower mass capture ratios for started mode, which also would be a conservative estimate, since higher mass capture ratios are desirable during operation. The other one-dimensional parameters are only weakly affected.

However, if the total temperature is doubled for wind tunnel ($T_\mathrm{w}/T_\mathrm{t} = 0.5$), which corresponds to a heated free stream, wind tunnel and flight mode predict nearly equal one-dimensional parameters at the throat. Furthermore, the predicted Mach numbers M_∞ for starting and unstarting coincide, although Reynolds numbers during wind tunnel mode are significantly higher than during flight mode. This result is conclusive with the observed Reynolds independence for starting and lower Reynolds numbers than present in the wind tunnel with $q = 1\ \mathrm{bar}$. If applied to real wind tunnel tests, these results suggest, that starting and unstarting can be accurately predicted in cold gas wind tunnels, if the correct ratio of total temperature to wall temperature is achieved.

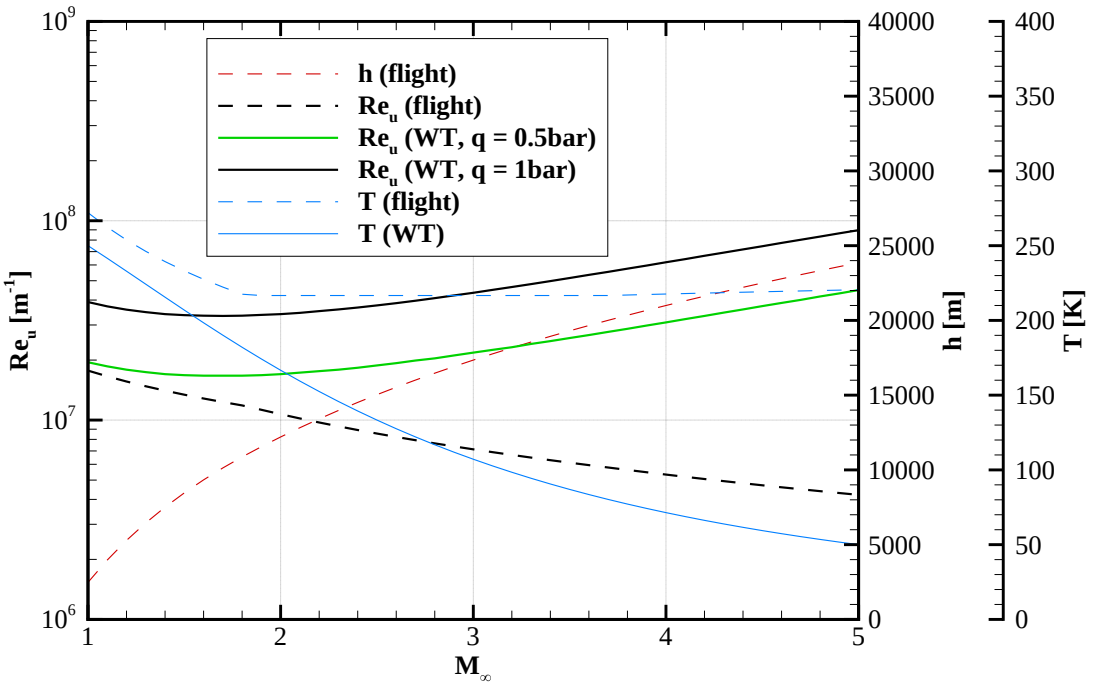

Figure 3.17: Free stream parameters for flight mode at $q = 0.524$ bar and wind tunnel mode

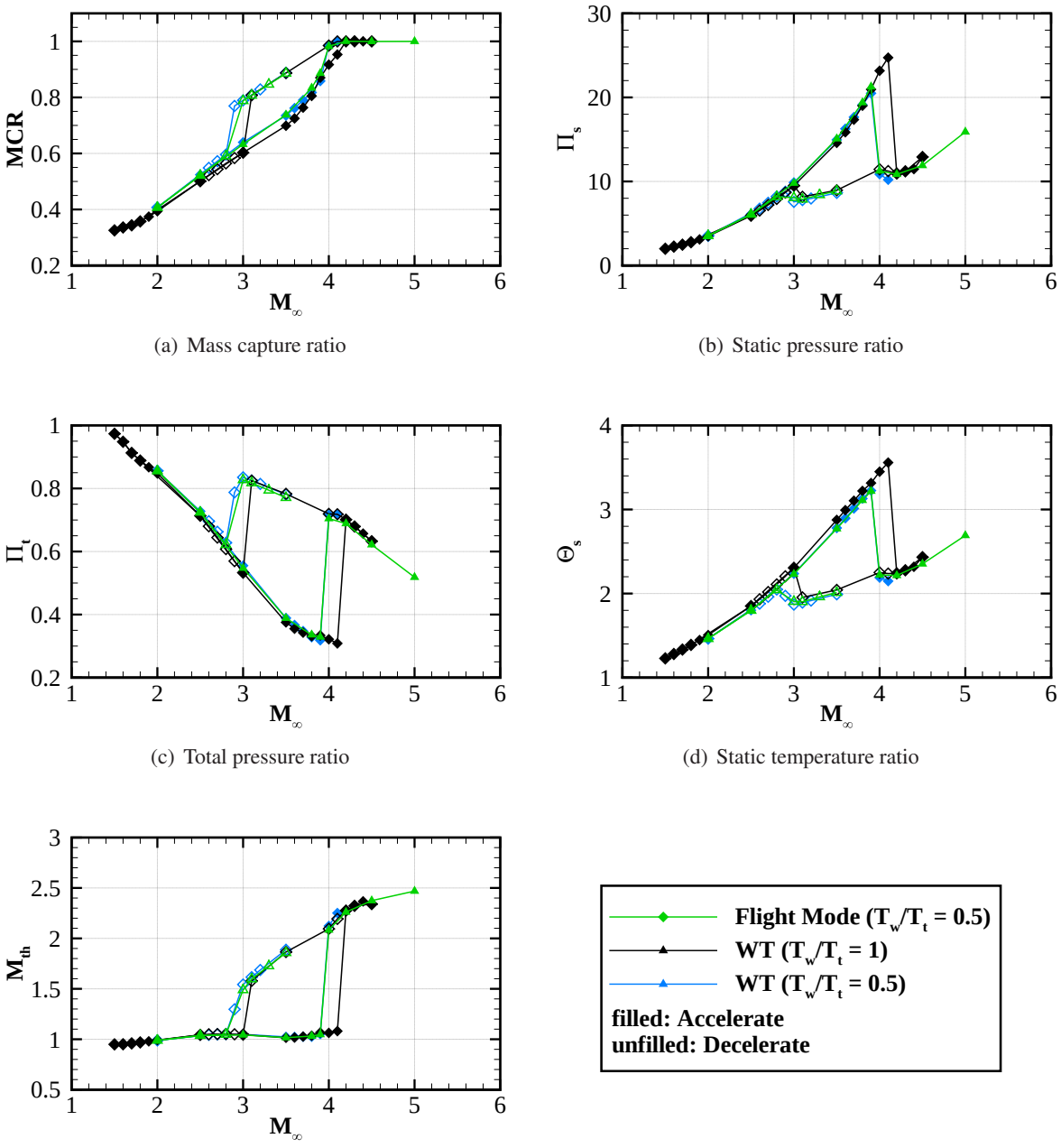

(a) Mass capture ratio

(b) Static pressure ratio

(c) Total pressure ratio

(d) Static temperature ratio

(e) Local Mach number

Figure 3.18: Influence of wind tunnel and flight mode on one-dimensional parameters for axisymmetric intake at A_{th}

4 Conclusion

Within this work, starting and unstarting of an axisymmetric Ramjet intake and two-dimensional Scramjet ramp intakes were studied numerically. For this purpose, a quasi-steady approach was developed, benchmarked against experiments and a parameter study was conducted.

The quasi-steady approach allowed to predict starting and unstarting with low computational effort. For each prediction, multiple steady runs were performed with incrementally varied free stream Mach number or angle of attack as independent parameter. The main focus of this work were viscous simulations with RANS turbulence models, that were complemented by Euler simulations. For the RANS simulations, a selection of one- and two-equation turbulence models were compared regarding their capability of reproducing experimental wall pressures. The analyzed models were the Spalart-Allmaras model, the k-ω model suggested by Wilcox and the shear stress transport model suggested by Menter. The SST model by Menter performed best at predicting the wall pressures, and was therefore selected for the RANS simulations.

The possibility to predict starting and unstarting with inviscid simulations was analyzed by comparing the RANS simulations with Euler simulations for a two-dimensional ramp intake. Euler simulations were not able to predict unstarting with separated boundary layer. Therefore, the prediction of critical cowl Mach number for starting was 81% higher, than predicted by viscous simulations. Unstarting, however, was predicted similarly by the Euler simulations with a difference of 5%.

The approach was benchmarked against experimental data of the axisymmetric intake, that was obtained from a study in the cold flow TMK-facility of DLR in Cologne by Dr. Dirk Herrmann and Mr. Martin Achner. The experiments were conducted at $M_\infty = 3.5$ and $M_\infty = 4$. During the experiments, the movable centerbody was traversed to adjust the internal contraction ratio CR_i and thereby cause the intake to start or unstart. The quasi-steady approach predicted critical cowl Mach numbers slightly higher for starting (8%) and unstarting (10%). The general effect of changed CR_i was same for experiments and CFD.

Within the parameter study, the effects of unit Reynolds number and relative wall temperature were analyzed for wind tunnel conditions. For this purpose, simulations with halved and doubled unit Reynolds number respectively relative wall temperature were conducted. The influence of the relative wall temperature were as following: Firstly, cooling of the wall leads to lowered cowl Mach numbers for starting by 5% and unstarting by 6%. Secondly, a heated wall increased the cowl Mach number for unstarting by 7% but did not alter the Mach number for starting. A similar effect was found for the unit Reynolds number: For increased unit Reynolds numbers, starting and unstarting were shifted to lower cowl Mach numbers by 10% resp. 3%. However, a decreased unit Reynolds number increased the Mach number for unstarting by 5% but did not affect starting. Consequently, starting seems to be independent of unit Reynolds numbers and relative wall temperature below a threshold unit Reynolds number and above a threshold for relative wall temperature.

Finally, the results obtained for wind tunnel conditions were compared to a flight trajectory with constant dynamic pressure of $q = 0.52$ bar and cooled wall, which led to slightly reduced cowl Mach numbers for starting (3%) and unstarting (5%) compared to wind tunnel conditions with adiabatic walls. As a consequence, these reference wind tunnel conditions gave slightly conservative estimates. If the same

relative wall temperature was applied in wind tunnel mode, the agreement to the modeled flight conditions was significantly increased. This suggests, that cold gas wind tunnel experiments can accurately predict starting and unstarting for these conditions, if the relative wall temperature is correctly modeled.

Within future works, the developed approach could be applied to further geometries to obtain further data of different contraction ratios and intake shapes. Additionally, determining the values of the observed thresholds for the influence of Reynolds number and relative wall temperature would benefit to predictions of starting and unstarting.

A Appendix

A.1 Exemplary input-file for RANS Simulations

```
    Files/IO ----------------------------------------: -
                            Boundary mapping filename: (thisfile)
                                Primary grid filename: tau.grid
                                  Output files prefix: hysteresis
                           Field output description file: (thisfile)
Surface output description file: (thisfile)
                       Automatic parameter update (0/1): 1
      Partitioning ------------------------------------: -
                                     Number of domains: 8
     Number of primary grid domains: 8
                              Type of partitioning (name): private
      Runtime optimisation ----------------------------: -
                    Cache-coloring (0/max_faces in color): 200000
  Axisymmetry (0/1): 1
Axisymmetry axial direction: 1 0 0
   Axisymmetry radial direction: 0 0 1
                             Bandwidth optimisation (0/1): 1
                        2D offset vector (0 / x=1,y=2,z=3): 2
 CFL number: 0.6
      Timestepping Start/Stop -------------------------: -
                                          Output period: 99999
  Surface output period: 99999
                                 Maximal time step number: 2000
                                          Minimum residual: 1e-8
      Monitoring --------------------------------------: -
                                    Monitor history (0/1): 1
                                      Field output values:
                        cp_mach_p_rho_temp_Ptot_gradrho_wdist
                                    Surface output values:
                        cp_mach_p_rho_temp_heatfl_yplus_bldelta_htc_ch_cfxyz_cf
                                       Monitoring values:
                        Rrho_Max-Rrho_Fx_Fy_Fz_Mx_My_Mz_Fx-v_Fx-p_C-lift_C-drag
      Geometry ----------------------------------------: -
                                             Grid scale: 1.0
      References --------------------------------------: -
                                    Reference Mach number: 4
                                    Reference temperature: 300
                                       Reference pressure: 1170
                                           Prandtl number: 0.72
                                       Gas constant gamma: 1.4
      Flux main ---------------------------------------: -
                        Inviscid flux discretization type: Central
                              Init total conditions (0/1): 0
      Turbulence --------------------------------------: -
                                Turbulence model version: SA
       IO ---------------------------------------------: -
    Reference system of forces and moments (tau/ln9300): tau
      Supersonic --------------------------------------: -
```

```
                          Flux carbuncle switch version: 1
  Multigrid indicator (0/1): 1
  Turbulence shock correction (0/1): 1
  Fix negative values (0/1): 1

 ------------------------------------------------------
 ADAPTATION
 ------------------------------------------------------
                                       Refinement mode: none
                                  Maximum point number: -1
                     Maximum point number per partition: -1
                               Percentage of new points: 100
                                 Adaptation sensitivity: 0.9
                                    Minimum edge length: 1e-12
                                         Indicator type: recon
                                  Indicator user-values: rho_mach_p
                                              Wanted y+: 0.8
                  Change wall normal distribution (0/1): 1
                                  #Minimum edge length: 1e-12


------------------------------------------------------------
------------------------------------------------------------

Minimum residual: 1e-5
CFL number: 0.5
Fix negative values (0/1): 0
Order of upwind flux (1-2): 2
Order of additional equations (1-2): 2



#---------------------------------------#
#    Case: Ma_4final.pval.90000
#---------------------------------------#

# Python script:
Primary grid filename: AxSym_Ma4_ref2.grid

# Python script:
Inviscid flux discretization type: Upwind

# Python script:
Time Step Smoothing Factor: 3

# Python script:
Turbulence model version: k-w

# Python script:
k-w model version: Menter_SST

# Python script:
Set gradients (0/1): 1

# Python script:
Number of domains: 8
```

```
# Python script:
Number of primary grid domains: 8

# Python script:
Reference Mach number: 4

# Python script:
Reference pressure: 8928.57142857

# Python script:
Reference temperature: 71.4285714286

# Python script:
Boundary mapping filename: Init.bmap

# Python script:
Minimum residual: 1e-12

# Python script:
Time Step Smoothing Factor: 0

# Python script:
Maximal time step number: 80000

# Python script:
CFL number: 1.5

    solver at Thu Jul 11 09:35:03 2019
Restart-data prefix: 0_Ma_4final.pval.90000
```

A.2 Exemplary BMAP-file for RANS Simulations

```
-----------------------------------------------------
 BOUNDARY MAPPING
 -----------------------------------------------------

            Markers: 1
   Type: supersonic inflow
               Name: Inlet
   Angle alpha (degree): 0
 block end
 ---------------------------

            Markers: 2
               Type: axisymmetry axis
               Name: Symmetry
 block end
 ---------------------------

            Markers: 3
               Type: viscous wall
   Subtype: turbulent
```

```
  Heat flux: isothermal
  Temperature: 300

              Name: Ramp
              Write surface data (0/1): 1

block end
--------------------------

           Markers: 4
              Type: exit-pressure outflow
              Name: Outlet

block end
--------------------------

           Markers: 5
              Type: viscous wall
  Subtype: turbulent
  Heat flux: isothermal
  Temperature: 300
              Name: Cowl
  Write surface data (0/1): 1

block end
--------------------------

           Markers: 6
              Type: viscous wall
  Subtype: turbulent
  Heat flux: isothermal
  Temperature: 300
              Name: Cowl_outer
  Write surface data (0/1): 1
  Monitor forces (0/1): 0

block end
--------------------------

           Markers: 7
              Type: exit-pressure outflow
              Name: Spillage
block end
--------------------------

           Markers: 8
              Type: farfield
              Name: Farfield
  Angle alpha (degree): 0
block end
--------------------------

           Markers: 9
              Type: axisymmetry wedge plane
              Name: Side1
block end
```

```
 ---------------------------

            Markers: 10
               Type: axisymmetry wedge plane
               Name: Side2
block end
 ---------------------------
```

A.3 Reference Mesh: General input-file

```
1 "curve based"
1 "zones"
1 "Main"
9 "groups"
1 "Curves" 1 1 0 0 1 1 0
2 "Inlet" 1 3 0 0 3001 1 0
3 "Symmetry" 1 3 0 0 2001 1 0
4 "Ramp" 1 1 0 0 3 1 0
5 "Outlet" 1 2 0 0 4001 1 0
6 "Cowl" 1 1 0 0 4 1 0
7 "Cowl_top" 1 1 0 0 5 1 0
8 "Spillage" 1 2 0 0 4002 1 0
9 "Farfield" 1 3 0 0 5001 1 0
25 "panels"
1 4
2 4
3 4
4 4
5 4
6 5
7 6
8 6
9 6
10 7
11 7
12 8
13 9
14 2
15 3
16 1
17 1
18 1
19 1
20 1
21 1
22 1
23 1
24 1
25 1
0 "periodic group pairs"
```

A.4 Reference Mesh: Surface input-file

```
1               !  Output Level(0-none, 1-normal, 2-detailed)
0               !  Desired number of surface triangles (0=off)
1.800000        !  Stretching ratio (1.5-2.1)
1.000000        !  Scaling parameter (0.25-4.0)

F               !  Use constant spacing
14.05588        !  Initial/Constant spacing value

0.8000000       !  Length Scale in absence of any features
0.1000000       !  Minimum Length scale for analytic curvature clustering

T               !  Activate interpanel curvature clustering
100.000 8.00000 !  Angle and factor for interpanel curvature clustering
6.000000        !  Factor for analytic curvature clustering interior to panels
2.000000        !  Factor for proximity clustering
7.000000        !  Factor for CAD clustering
```

A.5 Reference Mesh: Prism input-file

```
1               !  Output Level (0-none, 1-normal, 2-detailed)

F               !  Read in prismatic gap/cavity detection file (T/F)
0.4000000       !  Proportion of gaps to be filled by tets (0.2 - 0.8)
0               !  No. of passes for extending cavity area (0-4)

T               !  Automatic curve pullback activation(T/F)
100.000 0.330000 !  Min. angle(degrees) at curve for activation; ratio

15.00000        !  Ramp angle(deg)-- growth rate on final layer (5-30)

55              !  No. of prismatic layers to be generated (5-30)
0.0010000       !  Initial layer thickness (case dependent)
1.085000        !  Stretching factor (1.1-1.5)

F               !  Chop prismatic layers (T/F)
0.07320769      !  Minimum layer thickness (case dependent)

F               !  Use Enhanced Convex Area Treatment (T/F)
```

A.6 Reference Mesh: Tetrahedron input-file

```
1               !  Output Level(0-none, 1-normal, 2-detailed)
F               !  Restarting (T/F)?
1.670000        !  Stretching ratio (1.5-2.1)
1.000000        !  Scaling parameter (0.25-4.0)

T               !  Limit maximum tetrahedral size
30.00000        !  Maximum tet. length scale (if limit is True)

0.8000000       !  Thickness matching ratio(0.-1.)
```

```
1.900000        !  Tet./prism interface ratio(1.-3.)

9               !  Tet. Grid Quality (1-lowest -- 10-highest)
```

A.7 Reference Mesh: Source input-file

```
1
STARTGEOMSOURCE
"A_cl_Refinement" CIRCLE
50 0
-144.1994425 0 52.54954987
Surface RADIAL_STRETCHING 0.18 1.025
Tetra RADIAL_STRETCHING 0.18 1.025
ENDGEOMSOURCE
STARTGEOMSOURCE
"Ramp_Tip_Refinement" CIRCLE
35 0
-0.2581773188 0 0.09396951219
Surface RADIAL_STRETCHING 0.01 1.085
PrismInitial RADIAL_LINEAR 0.0005 0.001
ENDGEOMSOURCE
STARTGEOMSOURCE
"Cowl_Tip_Refinement" CIRCLE
22 0
-144.7018156 0 72.1277521
Surface RADIAL_STRETCHING 0.007 1.08
PrismInitial RADIAL_LINEAR 4e-05 0.0005
ENDGEOMSOURCE
STARTGEOMSOURCE
"Cowl_BLI_Refinement" QUAD
-166.2885234 0 85.29025061
-166.2885234 0 74.36779934
-568.2408437 0 85.88101831
-566.5970939 0 71.90915526
PrismInitial ABSOLUTE 0.0005
ENDGEOMSOURCE
STARTGEOMSOURCE
"Ramp_internal_Init_Thick" QUAD
-162.2731277 0 74.43031569
-162.2731277 0 50.75544504
-383.2383982 0 74.43031569
-383.2383982 0 50.75544504
PrismInitial BILINEAR 0.0005 0.0005 0.0009 0.0009
ENDGEOMSOURCE
STARTGEOMSOURCE
"Ramp_External_Init_Thickness" QUAD
5.696660072 0 4.106008358
-0.5743987466 0 -4.976216259
-170.7579945 0 67.46531706
-168.3793157 0 55.5719286
PrismInitial BILINEAR 0.0003 0.0003 0.0005 0.0005
ENDGEOMSOURCE
STARTGEOMSOURCE
"Cowl_Top_Rear" QUAD
```

```
-160.1755422 0 85.092444
-161.4097339 0 83.13316434
-165.4208636 0 88.16249566
-166.2539429 0 85.89466807
Surface ABSOLUTE 0.7
PrismInitial ABSOLUTE 0.0005
ENDGEOMSOURCE
STARTGEOMSOURCE
"Lip-Shock-BLI-Interaction" CIRCLE
13 0
-210.1224791 0 72.63100879
Surface RADIAL_STRETCHING 0.07 1.01
ENDGEOMSOURCE
```

Bibliography

[1] U.S. Standard Atmosphere, 1976. Technical report, National Aeronautics and Space Administration, 1976.

[2] Technical Documentation of the DLR TAU-Code Release 2014.2.0. Technical report, Deutsches Zentrum für Luft- und Raumfahrt e.V., 2014.

[3] J. D. J. Anderson. *Hypersonic and High Temperature Gas Dynamics*. AIAA Education Series, Reston, Virginia, 2nd edition edition, 1989.

[4] J. D. J. Anderson. *Modern Compressible Flow*. McGraw Hill, New York, 1990.

[5] J. D. J. Anderson. *Fundamentals of Aerodynamics, Second Edition*. McGraw Hill, Boston, 1991. ISBN 0071254080.

[6] J. D. J. Anderson. *Computational Fluid Dynamics - the Basics with Applications*. McGraw Hill, 1995.

[7] R. A. Baurle and R. L. Gaffney. Extraction of One-Dimensional Flow Properties from Multidimensional Data Sets. *Journal of Propulsion and Power*, 24(4):704–714, 2008.

[8] K. G. Bowcutt, J. D. J. Anderson, and D. Capriotti. Viscous Optimized Hypersonic Wavers. In *AIAA 25th Aerospace Sciences Meeting*, number 87-0272, 1987.

[9] J. Chang, N. Li, K. Xu, W. Bao, and D. Yu. Recent research progress on unstart mechanism, detection and control of hypersonic inlet. *Progress in Aerospace Sciences*, 89:1–22, 2017.

[10] H. Do, S.-k. Im, M. G. Mungal, and M. A. Cappelli. The influence of boundary layers on supersonic inlet flow unstart induced by mass injection. *Experiments in Fluids*, 51(3):679–691, 2011.

[11] P. Donde, A. G. Marathe, and K. Sudhakar. Starting in Hypersonic Intakes. In *42nd AIAA/ASME/SAE/ASEE Joint Propulsion Conference & Exhibit*, number July, 2006.

[12] A. K. Flock. *Design and Performance Analysis of Three-Dimensional Air Intakes for Supersonic Combustion Ramjet Engines*. PhD thesis, Universität Stuttgart, 2017.

[13] A. K. Flock and A. Gülhan. Modified kantrowitz starting criteria for mixed compression supersonic intakes. *AIAA Journal*, 57(5):2011–2016, 2019.

[14] A. Grainger, S. C. Tirtey, R. R. Boyce, S. Paris, and G. Paniagua. Starting Mechanisms for High Contraction Ratio Hypersonic Inlets. In *7th European Symposion on Aerothermodynamics*, 2011.

[15] W. H. Heiser and D. T. Pratt. *Hypersonic Airbreathing Propulsion*. AIAA Education Series, Washington D.C., 1994.

[16] R. Hermann. *Supersonic Inlet Diffusers and Introduction to Internal Aerodynamics*. Minneapolis-Honeywell Regulator Company, Minneapolis, Minnesota, 1956.

[17] O. M. Hohn. *Auslegung und Charakterisierung eines dreidimensionalen Scramjet-Einlaufs mit hohem Verdichtungsverhältnis und variabler Innenkontraktion*. PhD thesis, Universität Stuttgart, 2014.

[18] L. S. Jacobsen, C.-J. Tam, R. Behdadnia, and F. S. Billig. Starting and Operation of a Streamline-Traced Busemann Inlet at Mach 4. In *42nd AIAA/ASME/SAE/ASEE Joint Propulsion Conference & Exhibit*, number 2006-4508, pages 1–19, 2006.

[19] M. K. Jain and S. Mittal. Euler flow in a supersonic mixed-compression inlet. *International Journal For Numerical Methods in Fluids*, 50:1405–1423, 2006.

[20] A. Kantrowitz and C. duP. Donaldson. Preliminary Investigation of Supersonic Diffusers. *National Advisory Committee for Aeronautics*, 1945.

[21] S. Karl. *Numerical Investigation of a Generic Scramjet Configuration*. PhD thesis, Technical University Dresden, 2011.

[22] S. Lecheler. *Numerische Strömungsberechnung*. Springer Fachmedien, Wiesbaden, 2014.

[23] F. R. Menter. Two-Equation Eddy-Viscosity Turbulence Models for Engineering Applications. *AIAA Journal*, 32(8):1598–1605, 1994. ISSN 0001-1452. doi: 10.2514/3.12149.

[24] A. Najafiyazdi, R. Tahir, E. V. Timofeev, and S. Mölder. Analytical and Numerical Study of Flow Starting in Supersonic Inlets by Mass Spillage. In *Joint Propulsion Conference & Exhibit*, number July, 2007.

[25] H. Ogawa, A. L. Grainger, and R. R. Boyce. Inlet Starting of High-Contraction Axisymmetric Scramjets. *Journal of Propulsion and Power*, 26(6):1247–1258, 2010.

[26] K. Oswatitsch. Pressure Recovery for Missiles with Reaction Propulsion at High Supersonic Speeds. Technical report, Göttingen, 1944.

[27] H. Schade, E. Kunz, F. Kameier, and C. O. Paschereit. *Strömungslehre*. De Gruyter Studium. De Gruyter, Berlin and Boston, 4., neu bearbeitete auflage edition, 2013. ISBN 9783110292213.

[28] H. Schlichting. *Grenzschicht-Theorie*. Verlag G. Braun, Karlsruhe, 5th edition, 1965.

[29] R. Schwarze. *CFD-Modellierung*. Springer Berlin Heidelberg, Berlin, Heidelberg, 2013.

[30] M. K. Smart. Optimization of Two-Dimensional Scramjet Inlets. *Journal of Aircraft*, 36(2):430–433, 1999.

[31] M. K. Smart. Scramjets. *The Aeronautical Journal*, -(3219):605–619, 2007.

[32] M. K. Smart. How Much Compression Should a Scramjet Inlet Do? *AIAA Journal*, 50(3):610–619, 2012. doi: 10.2514/1.J051281.

[33] P. R. Spalart and S. R. Allmaras. A one-equation turbulence model for aerodynamic flows. In *30th Aerospace Sciences Meeting & Exhibit*, number January, Reno, Nevada, 1992. American Institute of Aeronautics and Astronautics.

[34] E. J. Stephen, S. R. Hoenisch, C. J. Riggs, M. L. Waddel, T. Mclaughlin, and M. A. Bolender. HIFiRE 6 Unstart Conditions at Off-Design Mach Numbers. In *53rd Aerospace Sciences Meeting*, number 2015-0109, 2015.

[35] B. Sun and K.-Y. Zhang. Empirical Equation for Self-Starting Limit of Supersonic Inlets. *Journal of Propulsion and Power*, 26(4), 2010.

[36] R. Tahir, S. Molder, and E. Timofeev. Unsteady starting of high mach number air inlets – a cfd study. In *39th AIAA/ASME/SAE/ASEE Joint Propulsion Conference and Exhibit*, Reston, Virigina, 2003. American Institute of Aeronautics and Astronautics.

[37] H.-J. Tan, S. Sun, and Z.-L. Yin. Oscillatory Flows of Rectangular Hypersonic Inlet Unstart Caused by Downstream Mass-Flow Choking. *Journal of Propulsion and Power*, 25(1):138–147, 2009.

[38] E. V. Timofeev, R. B. Tahir, and S. Mölder. On Recent Developments Related to Flow Starting in Hypersonic Air Intakes. In *15th AIAA International Space Planes and Hypersonic Systems and Technologies Conference*, number 2008-2512, pages 1–9, 2008.

[39] F. M. White. *Fluid Mechanics*. Mc Graw Hill, New York, 7th edition edition, 2011. ISBN 978-0-07-352934-9.

[40] D. M. V. Wie. Scramjet Inlets. In E. T. Curran and S. N. B. Murthy, editors, *Scramjet Propulsion*, pages 447–511. Progress in Astronautics and Aeronautics, 2000.

[41] D. M. V. Wie, F. T. Kwok, and R. F. Walsh. Starting Characteristics of Supersonic Inlets. In *32nd Joint Propulsion Conference*, number 96-2914, 1996.

[42] D. C. Wilcox. Reassessment of the scale-determining equation for advanced turbulence models. *AIAA Journal*, 26(11):1299–1310, 1988.

[43] D. C. Wilcox. *Turbulence Modeling for CFD*. DCW Industries, Inc., La Canñada, California, 1994.